Electrocatalysis

International Edition: DOI: 10.1002/anie.201504830
German Edition: DOI: 10.1002/ange.201504830

Earth-Abundant Nanomaterials for Oxygen Reduction

Wei Xia, Asif Mahmood, Zibin Liang, Ruqiang Zou, and Shaojun Guo**

Keywords:
electrocatalysts · fuel cells · nanostructure · oxygen reduction · platinum-free catalysts

Replacing the rare and precious platinum (Pt) electrocatalysts with earth-abundant materials for promoting the oxygen reduction reaction (ORR) at the cathode of fuel cells is of great interest in developing high-performance sustainable energy devices. However, the challenging issues associated with non-Pt materials are still their low intrinsic catalytic activity, limited active sites, and the poor mass transport properties. Recent advances in material sciences and nanotechnology enable rational design of new earth-abundant materials with optimized composition and fine nanostructure, providing new opportunities for enhancing ORR performance at the molecular level. This Review highlights recent breakthroughs in engineering nanocatalysts based on the earth-abundant materials for boosting ORR.

From the Contents

1. Introduction 2651
2. General Principle for ORR 2653
3. Pt-Based Multimetallic Nanostructures with Ultralow Pt Usage for ORR Enhancement 2655
4. Transition-Metal-Based Inorganic NPs for ORR 2656
5. Metal-Nitrogen-Carbon Catalysts for ORR 2661
6. Metal-Free Catalysts for ORR 2664
7. Inorganic Nanoparticle/Carbon and Carbon/Carbon Systems as Advanced ORR Catalysts 2667
8. Electrochemical Evaluation for ORR at the Microscale 2670
9. Conclusions and Outlook 2672

1. Introduction

Oxygen reduction describes a reaction in which an oxygen molecule receives electrons to form a product. This reaction is the cornerstone of many important energy-conversion devices, such as fuel cells and metal–air batteries, as well as some industrial processes like chlor-alkali electrolysis.[1] Among these application fields, fuel cells stand out because of their extraordinary prospects as future energy devices and solving some knotty problems that have long existed. Fuel cells have been considered as the most efficient and clean energy-conversion device in which fuels react with oxygen via mild electrochemical processes without combustion and the overall fuel-conversion efficiency is not limited by the Carnot cycle laws. The ideal thermodynamic efficiency of a H_2–O_2 fuel cell reaches about 83% at 25 °C, but direct utilization of H_2 in an internal combustion engine has a much lower efficiency of about 10–20%.[2,3] However, in practice, low-temperature fuel cells do not exhibit such efficiency mostly because of the sluggish oxygen reduction reaction (ORR) at the cathode.

In a fuel cell, the anode and cathode are separated by a membrane/electrolyte. Fuels, such as hydrogen, methanol, ethanol, or formic acid, are oxidized at the anode, giving off electrons that travel from the external circuit to the cathode. At the cathode, one oxygen molecule receives the desired four electrons and then is reduced to two water molecules or four hydroxy ions in acid or alkaline electrolyte, respectively. The electricity is finally generated through combining the anode and cathode reactions. Generally, in the typical H_2–O_2 fuel cells, the hydrogen oxidation reaction (HOR) at anode and ORR at cathode can be simplified as two half-cell reactions [Eq. (1,2)]:

$$\mathrm{HOR:}\ 2H_2 \rightarrow 4H^+ + 4e^-,\ E^0 = 0\ \mathrm{V}\ (\mathrm{vs.\ RHE}) \quad (1)$$

$$\mathrm{ORR:}\ O_2 + 4H^+ + 4e^- \rightarrow 2H_2O,\ E^0 = 1.23\ \mathrm{V}\ (\mathrm{vs.\ RHE}) \quad (2)$$

The kinetics of these two reactions are critical to the output performance of fuel cells. However, in low-temperature fuel cells both reactions are limited by huge activation energy barriers, which can be conquered with the assistance of catalysts inducing lower energy intermediates. Platinum (Pt) has long been the most efficient catalyst for both HOR and ORR. Owing to the slower kinetics in ORR (five-orders-of magnitude slower than that of HOR),[4] more Pt catalysts are needed in the cathode (about ten times more than that in anode).[5] There are some drawbacks hindering the widespread implementation of Pt-based catalysts in fuel cells. One lies in the very limited availability and high price of Pt (Figure 1) accounting for approximately 50% cost of a fuel-cell stack. Another challenging problem arises from the technical issue regarding the poor stability of Pt under operating conditions, such as dissolution, sintering, and agglomeration that result in the loss of performance.[6] Moreover, Pt-based catalysts are easily susceptible to a poor tolerance to methanol that would generate CO, blocking the active sites of Pt, and further leading to a mixed potential at the cathode. Rational design of extremely stable and alcohol-tolerant Pt-based nanomaterials with low Pt usage and non-Pt nanomaterials with close to or even higher ORR activity than Pt is thus at the heart of fuel-cell research.

Over the past decades, a tremendous amount of work has been devoted to dealing with the aforementioned problems,

[*] W. Xia, A. Mahmood, Z. Liang, Prof. R. Zou, Prof. S. Guo
Materials Science & Engineering, College of Engineering, Peking University
Beijing 100871 (P. R. China)
E-mail: rzou@pku.edu.cn
guosj@pku.edu.cn

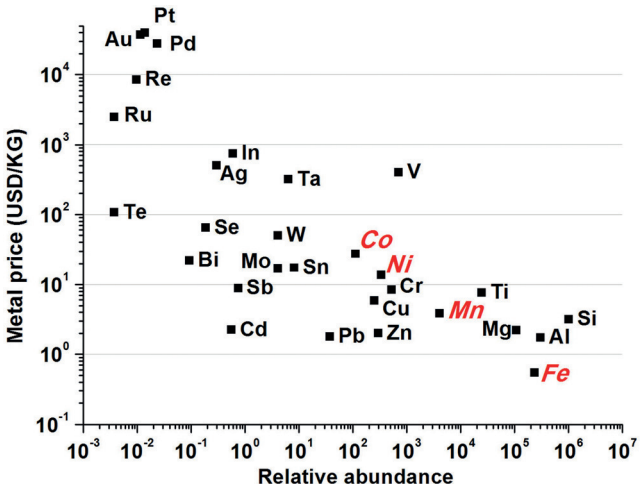

Figure 1. Relationship between metal price and its relative abundance in the Earth's upper continental crust (based on abundance of Si: 10^6 atoms). The metal price data on April 20, 2015 are from http://www.metal.com.

which can be mainly categorized into the following three main streams:

1) Tuning the size, shape, and structure of Pt nanostructures to optimize Pt utilization;
2) Designing PtM (M = transition metal)-based nanocrystals with controlled shape, composition, structure, strain and architecture to further enhance the ORR activity and stability;
3) Developing highly efficient alternatives based on earth-abundant elements, such as C, N, Fe, Co, Mn, for ORR enhancement.

Pt-based systems with new complexity have been thoroughly studied through in-depth experiments and theoretical simulation. The surface electronic, geometric, and strain effects of Pt-based nanostructures on ORR have been precisely controlled, leading to the enhanced and optimized performance.[7] Strategies and progress in fabricating Pt-based nanostructures for ORR have been summarized and thoroughly discussed in our previous work and some other recent Reviews.[8–12]

More interesting research has been directed towards rationally designing new non-Pt nanomaterials for improving the ORR activity and stability. By heavily doping with the active element, having high surface area, and special structure control, the newly developed earth-abundant materials can have a comparable ORR activity to Pt, but superior stability and methanol tolerance for ORR than Pt. However, there is still a big gap in ORR activity between non-precious nanomaterials and commercial Pt. This drawback can be partially resolved by considering adding more non-precious catalysts at the cathode for providing more active catalytic sites for ORR.

Wei Xia obtained his BS degree in Materials Science and Engineering from University of Science and Technology Beijing in 2011. Currently he is a Ph.D. candidate under the supervision of Professor Ruqiang Zou at the College of Engineering, Peking University. From March 2014 to July 2014, he joined Dr Anthony K. Burrell's group at the Argonne National Laboratory as a visiting scholar. His research interests include synthesis and application of porous materials in electrochemical energy storage and conversion.

Asif Mahmood received his BS degree in Chemistry from the Government College University Lahore in 2009 and his MS degree in Materials and Surface Engineering from the National University of Science and Technology, Islamabad, Pakistan, in 2011. Currently, he is working in Professor Ruqiang Zou's group at the College of Engineering, Peking University as a Ph.D. Scholar. His research interests involve porous materials for electrochemical applications including metal–organic frameworks, carbon and metal oxides.

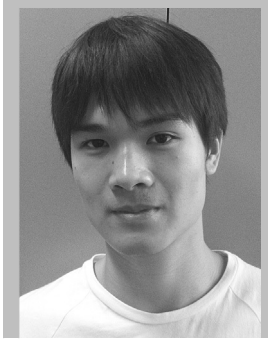

Zibin Liang is a student at the College of Engineering, Peking University, majoring in materials science and engineering. He has been working in Professor Ruqiang Zou's group since 2013. His research interests are the synthesis of functional carbon nanomaterials from metal–organic frameworks and their electrochemical applications as oxygen reduction reaction catalysts for fuel cells and metal–air batteries.

Ruqiang Zou is currently a Professor of Materials Science and Engineering at the College of Engineering, Peking University. He received his Ph.D. (2008) from Kobe University and AIST, Japan (JSPS Younger Scientist award). He was awarded a Director's Postdoc Fellow at the Los Alamos National Laboratory (USA). His research interests focus on the controllable preparation of hierarchically porous materials for hydrogen storage, carbon capture, and energy storage materials.

Shaojun Guo is Professor of Materials Science and Engineering at the College of Engineering, Peking University. He received his BS degree in chemistry from Jilin University (2005), and his Ph.D. from the Chinese Academy of Sciences (2011) with Profs. Erkang Wang and Shaojun Dong, and joined Prof. Shouheng Sun's group as a postdoc (Brown University). He then moved as J. Robert Oppenheimer Distinguished Fellow to the Los Alamos National Laboratory. His research interests are in engineering nanocrystals and 2D materials for catalysis, renewable energy, optoelectronics, and biosensors.

However, problems arise with the introduction of more catalyst into fuel cells, such as the limited space in an automobile and the increased weight, as well as a severe technical problem with regard to mass-transport property. For example, in a 10 μm thick Pt-based catalyst layer, the catalyst utilization is only 30–50 %.[13] A thicker catalyst layer would lead to the lower utilization. For this reason, the thicker cathodes with non-precious catalysts have not shown sufficiently high performance to date.[14] In this regard, it is highly desirable to design and tune new earth-abundant materials with new structures, doping with highly active elements, and having proper micropores/mesopores for improving the mass-transport, for greatly enhancing ORR performances in terms of activity, stability, and alcohol tolerance. However, controlled highly ORR-performance-oriented synthetic chemistry has long been absent.

In this Review, we mainly focus on recent breakthroughs in exploring highly efficient nanoelectrocatalysts based on the concept using of non-Pt elements for boosting ORR. However, before we delve into the earth-abundant ORR catalysts, a very short review of recent efforts in developing new strategies for highly active and stable Pt-based nanostructures for boosting ORR will be first presented to help the reader better understand what the current trends are in Pt-based nanosystems for ORR and why researchers would like to move to non-Pt systems for ORR with an activity close to or better than that of Pt. Significant advances in material sciences and nanotechnology stimulate researchers in designing and constructing highly efficient non-precious metal catalysts with advanced nanostructures and precise compositions, showing a bright future in replacing the Pt catalysts for fuel-cell application. In this Review, inorganic nanoparticles (NPs) with crystalline or amorphous phases will first be introduced as the new active and stable ORR catalyst. Then the nanostructured metal-nitrogen-carbon catalysts with enhanced ORR performance will be highlighted. After that, earth-abundant ORR catalysts, heteroatom-doped nanocarbons, such as CNT and graphene, will be discussed. The Review then introduces some exciting developments on the use of CNT or graphene/NPs as coupled catalytic systems for further enhancing ORR. Then, we will highlight recent new methods in estimating the ORR catalytic performance of earth-abundant nanocatalysts at the microscale. We finally conclude with a look at the future challenges and prospects of designs on new earth-abundant materials. Owing to the explosion of publications in this field, this Review article is not intended to be comprehensive, rather, we would like to discuss some salient features of recently highlighted important earth-abundant materials for boosting ORR.

2. General Principle for ORR

2.1. ORR Mechanisms

As shown in Equation (2), the thermodynamic equilibrium potential of ORR is 1.23 V, which means a zero net current at that point. A difference between the equilibrium potential and the experimentally applied potential, more often known as overpotential, is needed to drive the ORR process. The overpotential is directly linked with the fuel-cell efficiency, where a high overpotential would lead to the low efficiency.[3] Therefore, a highly efficient ORR catalyst can achieve the required current density under the low overpotential. However, even on the active Pt-based catalysts, a sufficiently high current is only observed at a large overpotential of more than 300 mV.[15] To improve the catalytic activity of ORR catalysts, a thorough understanding of the ORR kinetics is necessary but still a great challenge owing to the complex processes in ORR.

Equation (2) in the previous Section describes the overall reaction of the complete ORR process. However, under actual operating conditions, ORR has several elementary steps that involve multi-step electron transfer coupled or decoupled with proton transfer.[16–18] It is important to elucidate those ORR processes at the atomic level, which may help to identify the rate-determining step of the ORR kinetics and the origin of the overpotential. Early work has suggested a sequential reduction of oxygen on various electrode surfaces.[19] The predominant mechanism of ORR is schematically depicted in Figure 2. The oxygen molecule first diffuses to the electrode surface, forming an adsorbed oxygen molecule (O_2* where * denotes a site on the surface). After that, there are three pathways for the reduction of O_2*, which are distinguished by the sequence during the O–O bond cleavage step. The first pathway, named the dissociation pathway, is relatively simple, in it the O–O bond breaks directly to form an O* intermediate. Then the as-formed O* is reduced successively to OH* and to H_2O*. The second pathway is the associative pathway in which OOH* is first formed from O_2* and then the O–O bond is cleaved, generating the O* and OH* intermediates. The third pathway is the peroxo (or 2nd associative) pathway, in which O_2* is reduced successively to OOH* and to HOOH* (hydrogen peroxide on active site) before the O–O bond cleavage. Under different conditions, oxygen is reduced via different pathways, which can be estimated by the free-energy barriers. Density functional theory (DFT) simulations[20] show that the O_2 dissociative pathway has the lowest barrier at low oxygen coverage, and it dominates the ORR process. At high oxygen coverage, the associative mechanism with the lowest barrier is

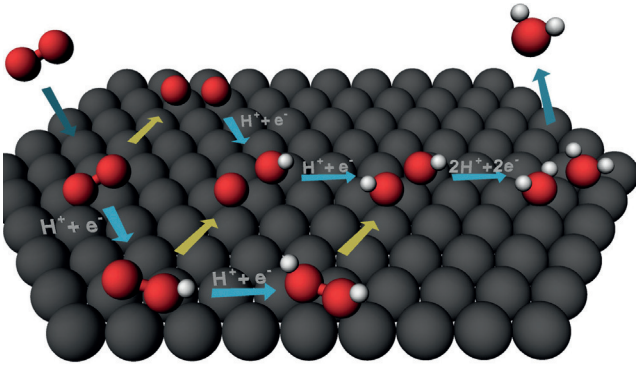

Figure 2. Proposed pathways for ORR. The black spheres represent catalyst atoms. The red spheres show the oxygen atoms and the white spheres are hydrogen atoms. The yellow arrows indicate O–O bond cleavage. The blue arrows show the proton or electron transfer.

the main ORR pathway. Moreover, the situation varies on different electrode materials.[20,21]

The adsorption of the intermediates (e.g. O*, OOH*, OH*) is a key to ORR kinetics. Direct experimental probes for these species are highly desirable to verify the mechanisms on various electrode surfaces, but it turns out to be very difficult.[22,23] Extraordinary progress has been achieved in computational studies, which have shown sufficient accuracy in verifying the energies of the surface interactions.[24,25] Through DFT simulation, Nørskov and co-workers suggest that the oxygen adsorption on the electrode is the origin of the overpotential. At high potential, oxygen adsorbed on the electrode surface is very stable, and the proton and electron transfer is impossible. The stability of the adsorbed oxygen is decreased by lowering the potential and the reaction can thus proceed. The binding energy of the oxygenated species to a given surface determines the catalytic activity. An optimal catalyst should have a moderate binding to the intermediates. If the adsorption on the electrode surface is too weak, then the electron or proton transfer to the adsorbed oxygen is limited. However, too strong an adsorption of O* or OOH* will lead to difficulties in H_2O desorption, which in turn blocks the active site for further oxygen adsorption. Volcano-shaped relations between the oxygen-reduction activity and the O*, OOH*, or OH* binding energy have been identified on a number of metal surfaces,[10,20] of these the Pt surface shows better binding to O*, OOH*, or OH* than those of earth-abundant metals, such as Fe, Co, Ni. Similar to the case of metallic catalysts, volcano-shaped relations have also been identified on non-metal materials, where N- or B-doped graphene can bind to the ORR intermediates neither too strongly nor too weakly, and thus exhibit higher activity than O-, P-, S-doped graphene or pristine graphene.[26] The intrinsic factor behind the different binding energy of the intermediates with various surfaces is their electronic structure. The higher the position of the metal d-states relative to the Fermi energy (the highest occupied state), the stronger the interaction of the electrode surface to the intermediates.[25] The optimal electronic structure with the proper binding energy of the intermediates will ultimately lead to better catalytic properties for ORR.

2.2. Electrochemical Evaluation of ORR catalysts

In evaluating the ORR performance of nanocatalysts, it is desirable to test them in a practical fuel cell by using membrane electrode assembly (MEA) and compare the different catalysts under identical operating conditions. However, in practice it is a significant challenge to exclude the influence from the different operating conditions as well as the distinct ways of fabricating the different catalyst layers. Moreover, this type of measurement shows the overall performance of the tested catalyst, bit gives no insight into the reaction mechanism on the catalyst surface.

These drawbacks in MEA could be compensated by the thin-film rotating disk electrode (RDE) and rotating ring-disk electrode (RRDE) measurements, in which catalysts are simply evaluated under well-defined conditions with less

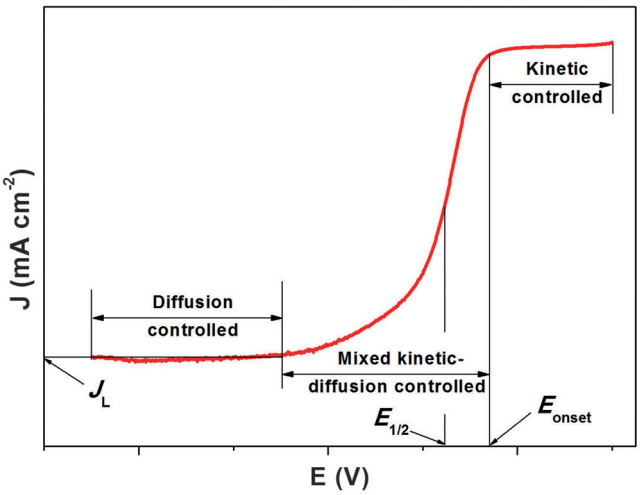

Figure 3. Typical ORR polarization curve.

disturbances. Figure 3 shows a typical ORR polarization curve of an individual catalyst. The curve can be divided into three parts in which ORR kinetics are controlled in different ways. In the kinetic-controlled area, the rate of ORR is quite slow and the current density increases slightly as the potential decreases. In mixed kinetic- and diffusion-controlled zone, the reaction accelerates as the potential drops, reflecting in a remarkable increase of the current density. In the diffusion-controlled zone, the current density is determined by the diffusion rate of reactants and reaches a platform at a certain rotating speed. Two parameters, onset potential (E_{onset}) and half-wave potential ($E_{1/2}$), can be read from the joint points of the three parts, which are usually used to verify the activities of catalysts qualitatively. The more positive is the potential value, the more active is the catalyst. However, the definitions of the E_{onset} vary from publication to publication. A potential value corresponding to 5% of the diffusion-limited current density (J_L) has been proposed as one definition for the onset potential.[27] A potential at which the current density exceeds a threshold value of 0.1 mA cm^{-2} was also suggested.[28] For cross-laboratory comparison, an identical standard is highly recommended; the definition of onset potential should at least be mentioned along with the potential value where they are compared with that of the so-called "state-of-the-art" Pt catalyst.

Kinetic current density (J_k) is another criterion in evaluating the activity of ORR catalysts. It can be obtained from the mass-transport corrected polarization curve though the Levich-Koutechky equation [Eq. (3)]:

$$1J = 1/J_k + 1/J_L \quad (3)$$

where J is the measured current density. The kinetic current densities of different catalysts are often compared at relatively high potential (e.g. 0.9 V vs. reversible hydrogen electrode (RHE) for Pt systems or 0.95 V for Pt alloy systems with very high activity), in which the inaccuracy of the mass-transport correction is relatively small.[29] Moreover, the interference from capacitive current density to the measured one should be considered to obtain the real ORR kinetic

current density. The interference can be minimized by lowering the sweep rates used in Pt-based catalysts. However, ion adsorption on the surface of some earth-abundant materials, such as porous carbons, is remarkable, which leads to the clear double-layer currents. The background contribution needs to be eliminated by subtracting the current density value of the N_2-based test from that of the O_2-based measurement.

The electron transfer number (n) and H_2O_2 intermediate production are also important parameters, which can be determined from RDE [Eqs. (3,4)] or RRDE results [Eq. (5)].

$$J_L = B\omega^{1/2} = 0.62nFC_0(D_0)^{2/3}\upsilon^{-1/6}\omega^{1/2} \quad (4)$$

$$4I_d = n(I_d + I_r/N) \quad (5)$$

where ω is the angular velocity, F is the Faraday constant (96485 C mol^{-1}), C_o is the oxygen bulk concentration, D_o is the oxygen diffusion coefficient in the electrolyte and υ is the kinetic viscosity of the electrolyte. I_d and I_r are the disk current and ring current in RRDE test, respectively, and N is the current collection efficiency of the Pt ring. The maximum energy capacity is achieved through four-electron reduction of oxygen to water. However, as mentioned above, a two-electron pathway leading to the formation of H_2O_2 in the ORR process, ultimately leads to a decrease in fuel-cell output.

3. Pt-Based Multimetallic Nanostructures with Ultralow Pt Usage for ORR Enhancement

In commercial polymer-electrolyte membrane fuel cells (PEMFCs), carbon-supported Pt NPs with the diameter of 3–5 nm are usually used as electrocatalysts and their ORR mass (0.11 A mg^{-1}) and specific activities (0.2 mA cm^{-2}) are usually significantly lower than those of the 2015 target of U.S. department of energy (U.S. DOE: 0.44 A mg^{-1} and 0.72 mA cm^{-2}). Furthermore, high cost of Pt hinders the large-scale application of PEMFCs where Pt amounts to around 55% of the total cost. To address these issues, recent significant advances on the reported new chemical syntheses of Pt-based nanostructures with different parameter-tuning capability provide new opportunities for achieving high ORR activities better or much better than the DOE 2015 target. In this Section, we will briefly highlight recent significant breakthroughs on how to engineer Pt-based nanostructures with control over their size, shape, composition, structure, strain, and architecture for significantly enhancing ORR. Figure 4 shows an outline of the major engineered Pt nanostructures (e.g. NPs, hollow NPs, intermetallic alloys, core/shell architectures, porous frameworks.) for boosting ORR.[30–33]

Alloying Pt with low-cost transition metals can lead to significant improvements in atomic and electronic structure as well as the available surface sites (ensemble effect), benefiting for tuning the binding strength of adsorbed species (reactants, products, spectator ions) with Pt. Figure 5 A shows

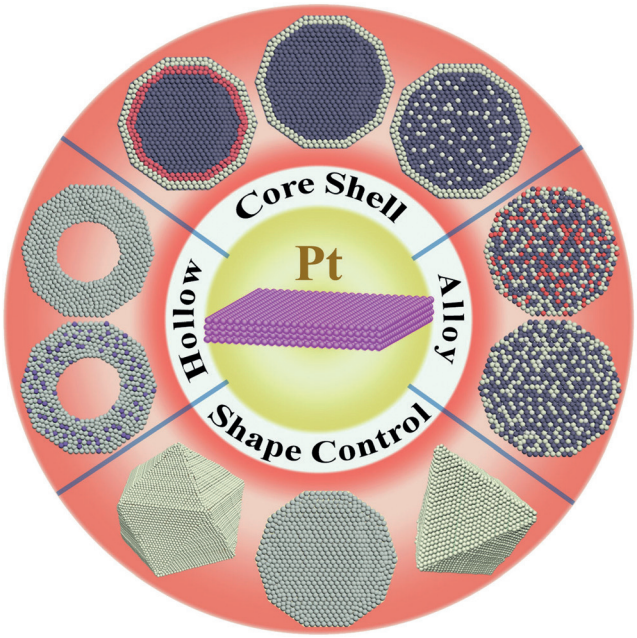

Figure 4. Recent important advances in new active and durable Pt-based nanostructures for improved ORR catalysis.

the measured activities of Pt alloys (Pt_3Ni, Pt_3Co, Pt_3Fe, Pt_3Sc, Pt_3Ti, Pt_3Y, Pt/Pd) and pure Pt as a function of oxygen adsorption energy as a volcano-like plot.[34] It shows that a surface that has 0.0–0.4 eV weaker oxygen binding energy than that of Pt(111) should have better ORR activity than Pt. It can be a nice guidance to tailor Pt-based alloy NPs for enhanced ORR catalysis. However, ORR proceeds in very harsh conditions (e.g. PH $\approx$ 0), causing selective leaching of transition metals from Pt alloys which affects the inherent ORR properties of Pt alloy NPs. This problem can be addressed by protecting Pt-alloy NPs with very thin Pt skin surface. Under the protection of multilayered Pt-skin surfaces, PtNi/Pt-skin particles show only 15% loss in specific ORR activity after 4000 potential cycles in 0.1 M $HClO_4$ solution at 60 °C, in contrast to 57% for the PtNi/Pt-skeleton and 38% for Pt NPs.[35] Besides the enhanced stability, the Pt-skin structure could also improve the catalytic activity for ORR. The PtNi/Pt-skin nanocatalyst exhibits improvement factors of more than 10 and 2 in ORR activity versus Pt and PtNi/Pt-skeleton catalysts, respectively. The driving force for the improved performance with the Pt-skin comes from electronic or strain effects. The presence of foreign metal atoms in the sub-surface modifies the electronic structure of Pt, resulting in weaker binding energies of reaction intermediates. Similarly, the presence of alloying species in the subsurface produce stresses in the Pt-skin surface, leading to altered adsorption kinetics.

To further enhance the ORR activity and durability, the disordered Pt-M alloy cores were replaced by the ordered Pt-M intermetallic cores. A simple wet impregnation coupled with a H_2 (5%)/N_2 (95%) reduction method was developed recently to obtain highly ordered intermetallic Pt_3Co core covered with 2–3 atomic-layer-thick Pt shell.[36] The developed intermetallic Pt_3Co exhibits a more than 200% increase

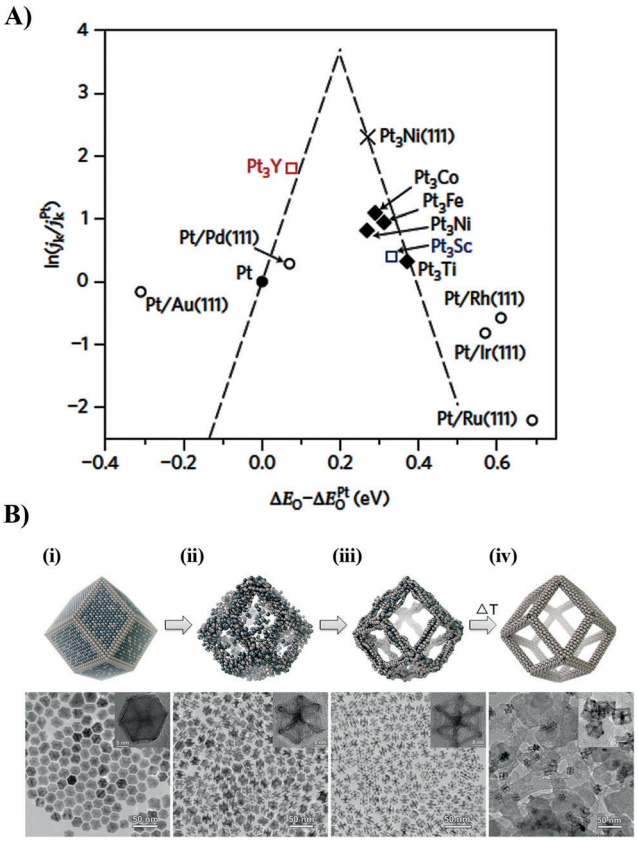

Figure 5. A) Volcano plots for the oxygen reduction reaction on Pt-based transition-metal alloys. Adapted from Ref. [34] with permission from the Nature Publishing Group. B) Schematic illustrations and corresponding TEM images of the samples obtained at four representative stages during the evolution process from polyhedral to nanoframes. i) Initial solid $PtNi_3$ polyhedra. ii) PtNi intermediates. iii) Final hollow Pt_3Ni nanoframes. iv) Annealed Pt_3Ni nanoframes with Pt(111)-skin-like surfaces dispersed on high-surface area carbon. Adapted from Ref. [41] with permission from the American Association for the Advancement of Science.

in mass activity compared with the disordered Pt_3Co alloy and a high stability up to 5000 cycles without any structural degradation. Similarly, a series of publications on FePt nanocatalysts show that the intermetallic FePt NPs with partially or even fully ordered face-centered tetragonal (fct) structure display much enhanced ORR activity and stability,[37,38] demonstrating an efficient and reliable approach to build better nanostructured ORR catalysts from Pt.

Pt alloy ORR catalysts can also be activated by controlling the catalysts through optimizing their shape, particularly a one-dimensional (1D) nanostructure is desired, in which the interaction between the catalytic alloy facet and the adsorbed oxygen as well as the carbon support is optimized. FePt and CoPt binary-alloy nanowires and FePtCu and FePtNi ternary-alloy nanorods have been developed for enhanced ORR catalysis.[39,40] To achieve the desired nanostructures, a precise control over the synthesis conditions (e.g. reactant, surfactant, temperature, time) should be reached. Moreover, the FePtM nanorods can be converted into core/shell nanostructures (FePtCu/Pt) by surface electrochemical dealloying, further enhancing ORR activity and durability.[40] The core/shell structure can be better tuned by seed-mediated synthesis, as demonstrated in the construction of core/shell FePtM/FePt (M = Pd, Au) nanowires.[33] An FePt shell with the thickness from 0.3 nm to 1.3 nm was grown in a controlled way over 2.5 nm wide FePtM nanowires to give the core/shell FePtM/FePt nanowires. These core/shell nanowires are generally more active and stable than the corresponding alloy nanowires. The best performing FePtPd/FePt nanowires (0.8 nm shell) achieve a high mass activity of 1.68 $A\,mg^{-1}$ Pt, which is almost 2 and 12 times that of FePtPd alloy and commercial Pt catalysts, respectively.

The growth of Pt-M alloys has been further extended to give high surface area interconnected three-dimensional (3D) networks which allow easier electrolyte access and better mass transfer capabilities. Recently, an easy and scalable method has been developed to synthesize highly controlled Pt_3Ni nanoframes.[41] Through the solution etching of Ni-enriched $PtNi_3$ nanopolyhedra (Figure 5B), the core of the polyhedra were selectively removed, and the edges could be well maintained. The resulting hollow Pt_3Ni nanoframes show a huge enhancement in the mass activity and specific activity by factors of 36 and 22 for the ORR, respectively, relative to state-of-the-art Pt/C catalyst.

Over the last decades, a number of Pt-based active and stable nanostructures, from core/shell NPs to Pt-M alloy frameworks, and to Mo-doped Pt-M alloy[42] have been realized in attempts to develop the ideal catalyst for ORR. The usage of Pt in efficient ORR catalyst has been remarkably decreased, however accompanied by an exciting improvement in catalytic activity. Hence, a good control over Pt nanostructure with efficient utilization of all the Pt atoms can provide breakthrough in ORR catalyst development for practical applications. However, the cost of Pt remains the major hurdle in the commercialization on a mass scale. Keeping in mind the cost issue, the development of catalysts based on non-precious metals or metal-free forms could provide the ideal way to overcome the cost issue and find a balance between cost and performance.

4. Transition-Metal-Based Inorganic NPs for ORR

To replace Pt-based catalysts for ORR catalysis, it is natural to consider some earth-abundant materials which have similar surface electronic properties to Pt. Inorganic NPs, such as tungsten carbide (WC), are such a choice, which have demonstrated promising ORR activity. The success of WC NPs in ORR catalysis stimulates the investigation of other metal carbides and other inorganic NPs including metal nitrides, metal oxides, and metal chalcogenides. Compared to metal carbides, metal nitrides are more stable during the ORR process, especially in acidic media. Metal oxides or sulfides are the most common form of inorganic nanocatalysts, which also displayed significant ORR activity. Recent breakthroughs in designing and synthesizing nanostructured transition-metal-based inorganic NPs further enhance their catalytic activity, offering a Pt-like catalytic activity toward ORR.

4.1. Metal Carbides

Metal carbides are of high interest for oxygen reduction and hydrogen evolution reactions owing to their good electrical conductivity and interesting electronic structure. Among them, tungsten carbide (WC) is especially promising because of its surface electronic properties which are similar to Pt.[43] The ORR reactivity of WC in acid environment was found to be superior than those of other transition-metal carbides, such as tantalum or titanium carbide (TaC or TiC).[44] However, the application of pure WC as an ORR catalyst for fuel cells is hindered by its low corrosion resistance in acidic or oxidative environments.[45] Addition of a second metal, tantalum (Ta) for example,[46] to the WC can improve its stability in acid electrolyte, which is attributed to the formation of W-Ta alloy in the catalyst. Moreover, the electrocatalytic activity was also enhanced owing to the presence of WC on the catalyst surface.

Ta is a highly corrosion-resistant metal. However, as mentioned above, the ORR catalytic activity of pure TaC is not sufficient. More often than not Ta is used to construct ternary systems for ORR catalysis. For example, Ta-Ni-C thin films prepared by magnetron sputtering, display significant ORR activity as well as good stability.[47,48] However, as can be seen from Figure 1, Ta is relatively rare and expensive among the transition metals and it should be considered as a minor component in the future ORR catalysis design.

Iron carbide (especially Fe_3C) is usually observed in Fe-N-C type ORR catalysts prepared from precursors that are rich in iron, nitrogen, and carbon.[49] During heat treatment, iron ions are reduced by carbon to form metallic Fe NPs via carbothermal reduction. At high temperatures, carbon atoms from the shells around the metallic Fe NPs diffuse into the Fe cores, leading to the formation of Fe_3C NPs. The merits of Fe_3C as a novel and promising ORR catalyst have been validated by a series of recent breakthroughs in constructing nanostructured Fe_3C-based electrocatalysts. Core/shell structured Fe/Fe_3C-C nanorods were prepared via a simple heat treatment on a mixture of cyanamide (NH_2CN) and $FeCl_3$.[50] The Fe/Fe_3C cores are encased in the nitrogen-doped graphitic carbon shell. The overall nanorod structure has a relatively uniform size with a diameter of 20–30 nm and a length of 1–2 μm. Energy-dispersive X-ray spectroscopy (EDS) measurement indicates that the nanorods are 48.5 wt% Fe, 45.2 wt% C, and 6.3 wt% N. ORR catalysis measurement shows that the Fe/Fe_3C-C nanorods outperformed the Pt/C catalyst. The Fe/Fe_3C-C displayed a kinetic current density of 26.89 mA cm^{-2} at 0 V (vs. Ag/AgCl) in neutral media, which is nearly twice as high as that of Pt/C (14.20 mA cm^{-2}). The activity of Fe/Fe_3C-C nanorods was attributed to the synergetic effects from the novel 1D core/shell structure and interactions between the Fe_3C core and the carbon shell.[50,51] The good activity and durability of Fe/Fe_3C-C catalysts in alkaline and acidic media have also been verified.[52–54] Given that metal carbide can dissolve in acidic solution, the good stability of Fe/Fe_3C-C samples in acid environment is attributed to the protection from the carbon shell.

Nevertheless, the role of Fe_3C in these composites toward ORR catalysis was ambiguous considering that the Fe_3C core encased by a carbon shell is not directly in contact with the electrolyte during the ORR process and the Fe/Fe_3C-C catalyst contains several electrochemical active species for ORR including metallic Fe, Fe_3C, nitrogen-doped carbon, and possible Fe_xN. To resolve this issue, Fe_3C-NP-decorated carbon nanospheres with negligible N or Fe content on the surface were developed for ORR catalysis study.[55] This complex was prepared by pyrolyzing a mixture of ferrocene and cyanamide in N_2 (Figure 6A). Scanning electron microscope (SEM) and transmission electron microscope (TEM) images show that the Fe/Fe_3C-C are uniform hollow spheres with a diameter of 400–500 nm (Figure 6B,C). Fe_3C NPs (ca. 10 nm) are uniformly embedded in the sphere. The Fe/Fe_3C-C catalyst displays considerable ORR activity and stability in both acid and alkaline media (Figure 6D,E). It is expected that the nitrogen and iron contents of the resultant material are high. However, X-ray photoelectron spectroscopy (XPS) results reveal negligible content of both atoms in the Fe_3C/C hollow spheres. For nitrogen, it is no more than 0.50 at% while the iron content is below 0.08 at%. The secret of this interesting phenomenon may lie in the pyrolysis process where the Fe_3C/C hollow spheres were obtained from a sealed autoclave with an auto-generated pressure of nearly 6.0×10^7 Pa (600 bar) at 700 °C. As a result, the observed high ORR activity was correlated with the Fe_3C NPs that might contribute by activating the surrounding carbon layers and making their outer surface active towards ORR.[55–57] The high-pressure pyrolysis methodology in this work could be an

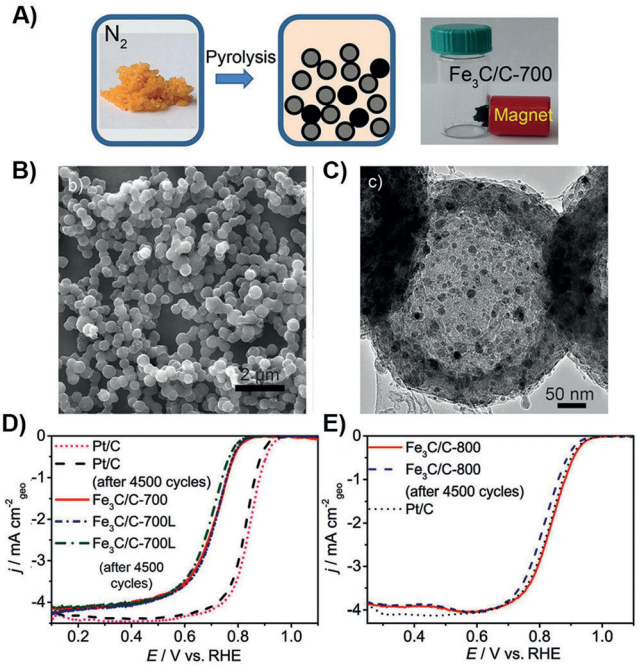

Figure 6. A) Synthesis of Fe_3C/C hollow spheres. B) SEM and C) TEM images of Fe_3C/C-700. D) ORR polarization curves of Fe_3C/C-700, Fe_3C/C-700L, and Pt/C at 900 rpm in 0.1 M $HClO_4$ before and after 4500 potential cycles. E) ORR polarization curves of Fe_3C/C-800 and Pt/C at 900 rpm in 0.1 M KOH before and after 4500 potential cycles. Adapted from Ref. [55] with permission from Wiley-VCH.

interesting and possibly efficient method to construct unusual nanostructures for ORR, however further in-depth study on how to introduce the low N and Fe contents on the surface of Fe_3C/C hollow spheres is highly desirable.

4.2. Metal Nitrides

Metal nitrides (MN_x, M = Mo, Co, Ti, Ta, etc.) are another new class of catalysts for ORR as a result of their excellent stability under harsh conditions (such as strong acidic electrolytes and high applied bias).[58] They are more difficult to etch at higher overpotential where most transition-metals tend to dissolve. Nitrogen can be easily inserted in the interstitial sites of early transition metals with negligible change to the crystal, which significantly improve the d-band structure. These changes can narrow the Fermi-level gap of transition metals compared with noble metals, leading to improved catalytic performance.[59] Furthermore, bonding of nitrogen with less electronegative elements (e.g. transition metals) leads to charge transfer in the resulting nitrides. This charge transfer activates the surface by producing acidic/basic sites for sorption of oxygenated species and modifying the d-band electron density, resulting in improvement of the catalytic response.[60] Several single-metal (TiN, CoN_x, Mo_xN_y, VN_x, WN_x, AlN)[61–66] and multi-metallic (Co-Mo, Co-W)[67,68] nitrides were designed and synthesized to improve the ORR performance. The potential electrocatalytic application of MN_x as an electrode in redox systems was identified for the first time by using TiN as a model in the basic electrolyte.[44] Subsequent work further explored the activity of TiN nanostructures on various substrates, such as carbon black, CNT, and graphene, with improved ORR activity.[61,69,70] Similarly, CoN NPs with a narrow size distribution of 7.5 nm (Figure 7A) were fabricated for ORR

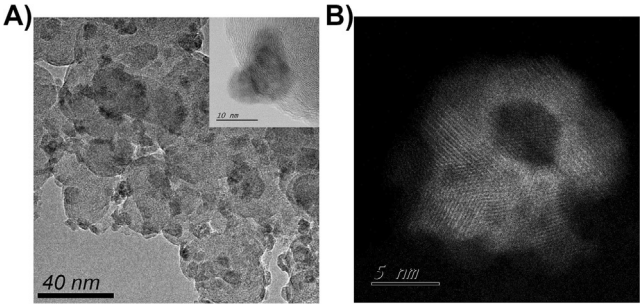

Figure 7. A) TEM image of porous CoN NPs supported on Vulcan XC-72 carbon. Inset: enlarged TEM image of a CoN NP. B) High-angle annular dark-field (HAADF) image of representative supported porous CoN NP. Adapted from Ref. [71] with permission from the Royal Society of Chemistry.

catalysis by refluxing an *o*-xylene solution of cobalt acetylacetonate ($Co(acac)_2$) and subsequent heat treating under NH_3.[71] The resulting CoN NPs, with a porous nanostructure (Figure 7B), undergo a four-electron transfer process in the alkaline electrolyte with an electrocatalytic activity remarkably similar to Pt. More recently, to find more active nitride-based catalysts for ORR, bimetallic nitrides were introduced to explore the synergistic effect of multimetallic species in the charge transfer for oxygen adsorption. The resulting $Co_{0.5}Mo_{0.5}N_y$ NPs are active with a high onset potential of 0.808 V vs. RHE and are very stable with a capacity retention of over 80% after 100 h for ORR in acid media, which is better than MoN or $Co_{5.47}N$.[67]

Metal oxynitrides ($M_xO_yN_z$) constitute another interesting system for developing efficient and durable ORR catalysts. Introduction of an O atom in a metal nitride may increase the surface defects that are critical to oxygen adsorption and consequently enhance the ORR activity of the resulting catalysts.[72] Several Ta, Zr-related oxynitrides have been investigated, showing improved ORR activity.[73,74] The use of TaO_xN_y particles for ORR shows that the presence of oxygen improves the catalytic activity of Ta_xN_y with a positive shift in the onset potential of nearly 400 mV in acid media.[73] Because the presence of multiple metal active species in the alloy structure can modify the d-band structure and the electronic states, multi-metallic oxynitrides were proposed as a way to further enhance ORR. They benefit from an optimized surface interaction with the oxygen molecule and with the oxygenated ORR intermediates which results in better ORR activity. One interesting example was recently demonstrated with Co-W-O-N NPs of the size of 3–5 nm. They exhibit a much improved onset potential of 0.749 V compared to monometallic Co and W oxynitrides in 0.5 M H_2SO_4.[68] More recently, bimetallic oxynitride $Co_xMo_{1-x}O_yN_z$ catalysts, controlled at the nanoscale (ca. 5 nm) by a solution impregnation strategy and subsequent by ammonolysis, exhibited an even higher ORR activity,[75] with E_{onset} at 0.918 V vs. RHE in alkaline media. These studies reveal that the rational design of metal nitride/oxynitride nanostructures with controlled size, shape, and structure may open new ways to generate highly efficient non-noble metal nanocatalysts for ORR that may be superior to Pt.

4.3. Metal Oxides

Metal oxides are promising alternatives to Pt-based catalysts considering their easy preparation, reasonable activity, and considerable stability in oxidative and alkaline environment. The drawbacks of metal oxides for ORR catalysis are their intrinsically large band gap that in turn causes poor apparent electrical conductivity and weak oxygen sorption on metal oxide surface. Extensive efforts have been devoted to making the nanostructured metal oxides to improve their catalytic activities.

Cobalt and manganese oxides are the most studied metal oxides for ORR catalysis. Cobalt oxides, including CoO and Co_3O_4, display much enhanced ORR activity when they are nanostructured, analogous to Pt structure engineering, as depicted in Figure 4. Size-dependent ORR activity in cobalt oxides was observed in a series of CoO NPs with average sizes of 3.5, 4.9, and 6.5 nm.[76] The smaller CoO NPs show higher ORR activity than the larger one, which however is found to be independent of the turnover frequency (TOF) on NPs but

instead correlates with the richer interface between the smaller Co NPs and the carbon support. Morphology control is also efficient in enhancing the catalytic activity of NPs. Co_3O_4 nanorods show higher activities toward ORR than NPs,[77] which is caused by the fact that nanorod can provide a higher density of surface-exposed Co^{3+} ions. A number of cobalt oxides were fabricated with advanced nanostructures including ordered mesoporous,[78] core/shell,[79–81] and hollow architectures,[82,83] showing excellent mass transport properties and enhanced activities for ORR. The (110) facets in Co_3O_4 catalysts are particularly active. However, bulk Co_3O_4 single crystals usually have a low proportion of this facet, thus leading to low catalytic activity. Recently, polycrystalline Co_3O_4 hollow NPs, with a high proportion of exposed (110) facets, were introduced as an advanced nanocatalysts for ORR.[82] For the preparation of such a structure, monodisperse ε-Co NPs were first prepared by decomposing $Co_2(CO)_8$, and then oxidized at 230 °C for 2 h. The size of these Co_3O_4 NPs with a hollow structure increases from 10.7 ± 1.0 nm to 14.8 ± 1.3 nm. Thin films assembled from these Co_3O_4 hollow NPs demonstrate a good catalytic activity for both ORR and OER. Furthermore, the catalytic activities and stabilities of cobalt oxides, as well as other oxides, can be further enhanced when coupled with advanced conducting substrates, such as carbon nanofibers,[84] CNTs,[85,86] and graphene.[87,88] Details will be presented later.

The idea of designing manganese oxide based ORR catalysts is similar to that of cobalt oxides. Manganese oxides include more complex members, such as MnO,[89,90] Mn_2O_3,[91,92] Mn_3O_4,[93,94] MnO_2,[95,96] Mn_5O_8, and MnOOH.[97,98] The activity of these manganese oxides varies, usually depending largely on the electronic states, and following the sequence: $Mn_5O_8 < Mn_3O_4 < Mn_2O_3 <$ MnOOH.[97] The exact difference between different manganese oxides is more related to the reduction of Mn^{4+} to Mn^{3+} and the following electron transfer step of Mn^{3+} to oxygen.[99,100] Other metal oxides, such as Fe-, Cu-, Ti-, Zr-, Ta-, Nb-, and Sn-based oxides were also evaluated as new ORR electrocatalysts,[101–110] however, unfortunately show lower activities than Co- or Mn-based oxides.

In addition to the single-component metal oxides, perovskite-type mixed-metal oxides represent a more highly promising earth-abundant material for ORR because of their better properties, such as high electrical conductivity and very high chemical stability. The general formula for perovskite-type oxides is ABO_3 (A = La, Ca, Sr, or Ba, and B = Ni, Co, Fe, Mn, or Cr; Figure 8A).[111] The catalytic activity of these materials is largely dependent on the B sites. The neither too strong nor too weak interaction of the B site with the surface-adsorbed oxygen species is crucial for enhancing ORR activity. The A sites primarily contribute to the stability of overall structure. The catalytic properties can be tailored by partial substitution of the A or B sites with a third cation, making them a unique platform for the development of optimal ORR catalysts.[112–115] An important progress regarding the perovskite metal oxide catalysts was made with the introduction of a general design principle for enhancing their ORR activity.[116] The extent of σ*-antibonding (e_g) orbital occupation and B-site transition-metal–oxygen covalency

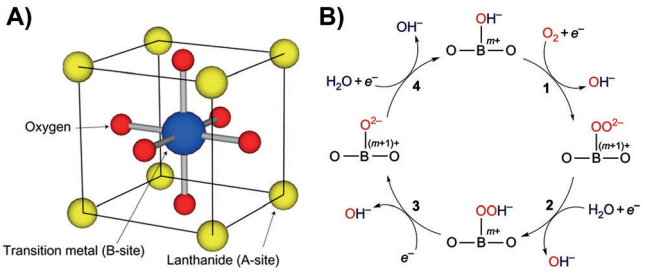

Figure 8. A) ABO_3 perovskite structure model. B) Proposed ORR mechanism on perovskite oxide catalysts. The interaction of the B-site to oxygen is critical to ORR activity. If the interaction is too weak, step **1** is unlikely to occur. If the interaction is too strong, step **2** will be prohibited. Adapted from Ref. [116] with permission from the Nature Publishing Group.

were found to govern the ORR activity (Figure 8B). It demonstrates good prospects for developing highly active ORR catalysts by tuning these surface electronic structure features of perovskite-type oxides.

Spinel-type oxides (AB_2O_4) are another important class of mixed-metal oxides for ORR catalysis. Particularly, the Co-based spinel oxides, with partial Mn, N, or Cu substitution, show great potential in enhancing ORR activity.[117,118] Some $MnCo_2O_4$ catalysts even outperform Pt/C for ORR catalysis in terms of the current density at medium overpotentials and the stability in alkaline media.[119] Bearing the benefit from well-defined nanostructures in mind, researchers have tried to modify the microstructure of spinel oxides to obtain better catalysis performance. A reduction-recrystallization methodology has been developed for rapid room temperature synthesis of nanocrystalline spinels from amorphous MnO_2.[120] A more precise control over the size of spinel nanocrystal was fulfilled by the solution phase synthesis, where a series of $MxFe_{3-x}O_4$ (M = Fe, Cu, Co and Mn) NPs were prepared with uniform diameter of 7 ± 0.2, 8 ± 0.3, 5 ± 0.2, and 5 ± 0.2 nm, respectively (Figure 9). Such a structure provides sufficient surface redox-active sites for oxygen adsorption and activation, leading to a highly efficient ORR catalyst. Particularly, $MnFe_2O_4$ NPs display high activities toward ORR, which are comparable to that of Pt NPs in alkaline solution.[121]

Amorphous metal oxides are a new type of material that deserves special attention. The long-range disorder in amorphous oxides suggests the possible existence of unusual bonding arrangements that can be beneficial for electrocatalysis.[122] Actually, amorphous metal oxides have displayed competitive catalysis activity to the crystalline counterparts, and may outperform the crystalline metal oxides in terms of the ORR activity and stability. For instance, amorphous manganese oxide with the molecular formula of $Na_{0.10}MnO_{1.96}{\cdot}0.7H_2O$ was prepared by treating sodium permanganate with disodium fumarate at ambient temperature with the addition of a small amount of H_2SO_4 that was used to induce the disproportionation reaction of Mn^{4+} to MnO_2 colloidal NPs and Mn^{2+}. The as-prepared amorphous manganese oxide has much more structural distortion, thus possibly more active sites for oxygen adsorption and activa-

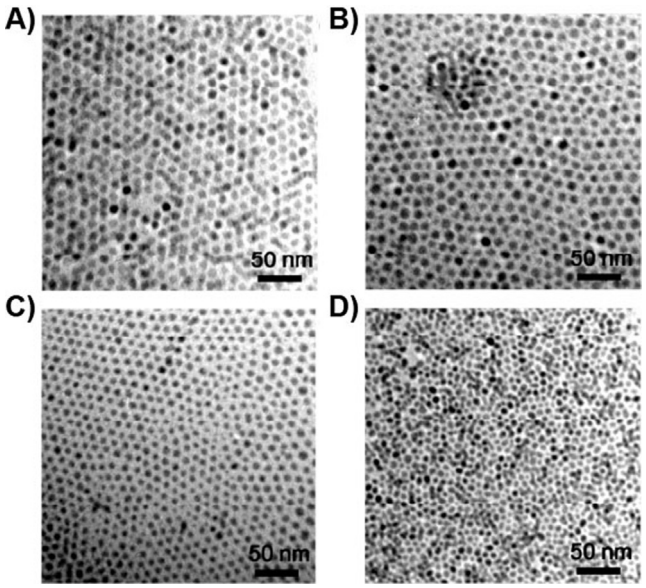

Figure 9. TEM images of the as-prepared A) Fe_3O_4, B) $Cu_{0.7}Fe_{2.3}O_4$, C) $Co_{0.8}Fe_{2.2}O_4$, and D) $Mn_{0.4}Fe_{2.6}O_4$ NPs. Adapted from Ref. [121] with permission from the American Chemical Society.

tion than its crystalline counterpart does. Moreover, the amorphous manganese oxide has an advanced nanoporous structure for better mass diffusion than the dense and crystalline manganese oxide. These important characteristics can contribute to the reasonable ORR activity for amorphous metal oxides.[123,124] Mixed-metal oxides with amorphous phases exhibit even better performances for ORR. To make this kind of complex, a mixture of $CoCl_2{\cdot}6H_2O$, $Fe(NO_3)_3{\cdot}6H_2O$, and KOH in tertiary butanol solution was allowed to react at 160 °C for 1 h to give the amorphous cobalt iron oxide ($CoFe_2O_n$, $n \approx 3.66$).[125] Alternatively, by using water as the reaction solution and increasing the reaction time to 6 h, the highly crystalline counterpart ($CoFe_2O_4$) was obtained. Figure 10 A,B are the typical TEM images of the crystalline and amorphous cobalt iron oxide, where $CoFe_2O_4$ displays clear lattice fringe corresponding to the (111) plane of cubic $CoFe_2O_4$ while $CoFe_2O_n$ shows an amorphous phase. The selective area diffraction pattern also reveals the amorphous nature of $CoFe_2O_n$, consistent with the XRD result (Figure 10 C). Figure 10 D shows the ORR polarization curves of the amorphous $CoFe_2O_n$, crystalline $CoFe_2O_4$ and commercial Pt in 0.1 M KOH. $CoFe_2O_n$ demonstrates a significantly higher onset potential and a larger current density than the $CoFe_2O_4$, and its diffusion limiting current density is even higher than that of Pt. From the very limited work on amorphous metal oxides for ORR catalysis, we can find a general principle for preparing highly efficient amorphous ORR catalysts. That is, the use of the relatively low temperature and short reaction time during the synthesis of amorphous metal oxide nanostructures can introduce the high density of defects that aid improved oxygen adsorption and activation. Nevertheless, the exact origin of the enhanced ORR activity in amorphous metal oxides has not been resolved. In-depth studies on the structure of these materials are necessary before a general conclusion can be made on how to design amorphous metal oxides for future ORR catalysts with improved activity and stability.

4.4. Metal Chalcogenides

Metal chalcogenides (M_xCh_y, M = Co, Fe, Ni, Ir, Ru, and Ch_y = S, Se, Te) have a unique cluster-like crystal structure formed by interaction between central metal with non-metallic elements (chalcogen atoms). The formation of these clusters may provide a good reservoir for electron transfer from catalyst to adsorbed oxygen during catalysis. And also, the chalcogenization can lead to changes in the surface chemistry of the metals and prevent the oxidative poisoning of the as-prepared electrocatalysts.[126] In particular, metal chalcogenides are more stable in the acidic electrolyte than metal oxides. These important properties of metal chalcogenides may provide a new platform for improving the ORR performance. Since the early finding of ORR

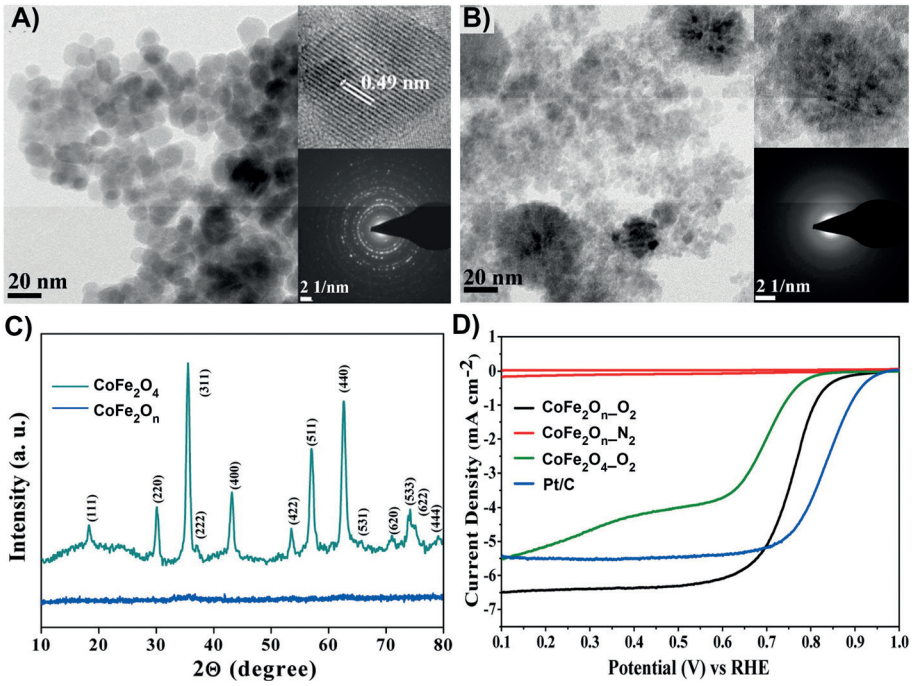

Figure 10. TEM images of the A) crystalline $CoFe_2O_4$ and B) amorphous $CoFe_2O_n$. Inset: higher resolution image and diffraction pattern. C) Powder XRD patterns of $CoFe_2O_4$ and $CoFe_2O_n$. D) ORR polarization curves of crystalline $CoFe_2O_4$, amorphous $CoFe_2O_n$ and 20 wt% Pt/Vulcan X-72 in 0.1 M KOH. Adapted from Ref. [125] with permission from the American Chemical Society.

activity in a Co–S system,[127] non-precious-metal chalcogenides have been widely explored as potential candidates for ORR. The trends for ORR activity by the use of non-precious-metal chalcogenides are that S^{2-} and Co^{2+} are the best anion and cation for ORR, respectively, with the activity decrease as follows: S > Se > Te and Co > Ni > Fe.[128] With this knowledge, the synthesis of cobalt sulfide-based nanostructures is the most promising to get more active and stable catalysts for ORR. Hierarchical hollow Co_9S_8 microspheres with large surface area, synthesized by a simple solvothermal method in a binary solution of triethylenetetramine and water, show a high ORR activity with an onset potential of 0.88 V vs. RHE, much higher than the predicted value (0.74 V) from previous theoretical simulation.[129] To enhance the conductivity of cobalt sulfide, recently, graphene was used as an advanced conductive support to disperse $Co_{1-x}S$ NPs to obtain a highly active ORR catalyst.[130] The composite catalyst shows a high onset potential of 0.8 V vs. RHE in H_2SO_4 solution.

Alloying cobalt sulfide with another transition metal is another approach to further enhance the ORR performance of cobalt sulfide materials. This has been well demonstrated in the synthesis of urchin-like NiCo sulfide sub-micron spheres and highly active nitrogen-doped carbon/CoFe sulfide NPs composite for boosting ORR.[131,132] In particular, carbon/CoFe sulfide NPs composites can have the very high onset and half-wave potentials of 0.913 V and 0.808 V vs. RHE and large current density (e.g. 4.7 mA cm^{-2} at 0.7 V) in alkaline media, much better than that of carbon/Co sulfide (3.9 mA cm^{-2} at 0.7 V), which highlights the importance of the alloy effect in enhancing ORR.

5. Metal-Nitrogen-Carbon Catalysts for ORR

5.1. Transition-Metal Macrocycle and Organic/Transition-Metal-Precursor Derived ORR Catalysts

The early work in metal-nitrogen-carbon (M-N-C) type electrocatalysts dates back to 1964 when Jasinski who found that a N_4-chelate complex with a cobalt metal center was active for ORR catalysis.[133] Since then, many macrocycle molecules, with the general feature of having transition-metal centers (Co, Fe, Ni, or Mn) coordinated to four surrounding nitrogen atoms, have been investigated. These materials include porphyrins, phthalocyanines, tetraazaannulenes, and their derivatives with substituent functional groups. The reactivity of these materials was believed to correlate with the electronic configuration of the metal centers. Charge transfer from the electron-rich metal center to O_2 π^* orbital was suggested to lead to a weakened O–O bond, thus enhancing ORR.[134] Despite its good prospects, transition-metal-macrocycle-mediated ORR only proceeds well in alkaline solution. It was found to have poor activity and stability for ORR in acidic media, but that changed when researchers later found that simple heat treatment over these materials could efficiently improve their stability as well as the activity.[135,136] Further studies show that the expensive transition-metal macrocycles were not necessary to produce the M-N-C catalyst by heat treatment. A more cost-effective methodology was developed by pyrolyzing the mixture of a simple nitrogen-rich molecule and a transition-metal salt with or without carbon support.[137,138] The materials obtained from this route have a competitive ORR performance for practical fuel-cell applications.[139,140]

Although catalysts with considerable ORR activity can be prepared from the pyrolysis route, particularly in the presence of Fe or Co, a clear understanding of the coordination change or structure evolution during the heat treatment process is absent. The nature of the active sites in these pyrolyzed samples is also under debate. Fe, coordinated with two, four, or six N atoms, was suggested as the active centers.[141,142] However, in some cases metal species were proposed not to participate in catalysis as direct active sites. Instead, they contribute by catalyzing the formation of active sites (e.g. pyridinic and quaternary nitrogen atoms in the carbon plane).[143,144] As shown in Figure 11, a number of species were proposed to result from the heat treatment of cobalt and manganese N_4-metallomacrocyclic complexes, such as M–N_x moieties, metal, metal oxides, and nitrogen-functionalized carbon groups.[145] The overall ORR performance of the product was attributed to the simultaneous and interactive presence of these components.

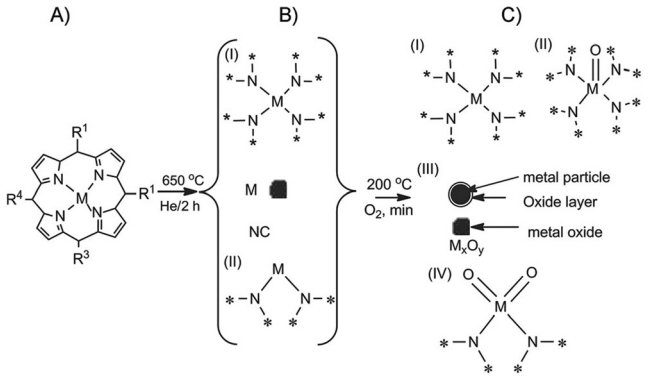

Figure 11. Schematic illustration of the possible groups that are formed during pyrolysis of cobalt and manganese N_4-metallomacrocyclic complexes. Adapted from Ref. [145] with permission from Wiley-VCH.

It is worth noting that metallic species, such as Fe, Co NPs often exist in M-N-C catalysts. Though they were reported as being less active than nitrogen-coordinated metal centers, the contribution from these metal NPs should not be ignored. Fe or Co NPs are highly active and can be oxidized even under ambient conditions. The resultant metal oxides, as discussed in the previous Section, are highly active toward oxygen reduction when coupled with an electrical conducting matrix (N-doped carbon in this case). Thus, in the study of M-N-C type ORR catalysts, the contribution made by the probable presence of surface metal oxides needs to be considered or even utilized to build better catalytic systems.

5.2. Nanostructuring Metal-Nitrogen-Carbon Catalyst

Without a clear understanding of the active sites in these catalysts, efforts to form better catalysts by simple composition adjustment are, to some extent, based on guesswork. It is difficult to predict the ideal composition for an M-N-N type catalyst. Nitrogen content, for example, does not necessarily govern the ORR activity. A balance between the nitrogen content and nitrogen species needs to be identified experimentally before a good performance can be obtained.[146] However, we can still find some general features that might be of great help in designing better ORR catalysts. Tuning the electrocatalysts on the nanoscale to give a high surface area and many mass transport pathways, which determines the amount of accessible active sites and exchange of ORR-related species (O_2, H^+ or H_2O), is perhaps the most straightforward strategy to enhance their ORR activities without changing the intrinsic TOF. However, the normal pyrolysis of simple macrocycles or mixtures of nitrogen and metal precursors only leads to uncontrolled agglomeration or inhomogeneous microstructure and thus insufficient exposure of the active sites and poor mass transport.[147] Rational design on the precursors and of the heat treatment parameters is thus critical to obtain the desired structures for enhanced ORR catalysis.

From this perspective, hard-template synthesis is a general and efficient route to construct M-N-C catalysts with well-controlled porous nanostructures. Silica colloid, ordered mesoporous silica SBA-15, and layered montmorillonite with 2D open channels are three typical hard templates with distinct structures (Figure 12). Vitamin B12 (VB12) or

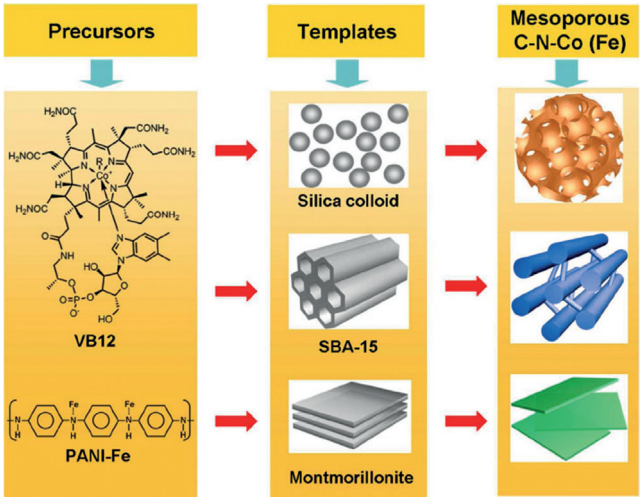

Figure 12. Templating synthesis of mesoporous C-N-Co (Fe) catalysts. Adapted from Ref. [148] with permission from the American Chemical Society.

a polyaniline Fe complex as M-N-C precursors were loaded into these templates and converted into Co-N-C or Fe-N-C materials with well-defined mesoporous structure and high BET surface area of up to 572 m^2g^{-1}.[148] As a result, these catalysts display much improved activity toward ORR than those without nanostructuring. The most active catalysts from VB12 precursor and silica colloid templates exhibit comparable ORR activity and selectivity to Pt/C in acidic electrolyte (half-wave potential of ca. 58 mV deviation from Pt/C; electron-transfer number over 3.95).

Despite the universal adaptability and promising ORR performance of the resultant catalysts, this hard-template route requires intricate processes including the infiltration of precursors and removal of template. As such, we turn to soft-template means for tuning the nanostructures to enhance ORR catalysis. A typical surfactant Plutonic P123 (PEG–PPG–PEG) was mixed with conventional M-N-C precursors melamine, $Fe(NO_3)_3$, and then heated to 800 °C in several steps over 1 h (Figure 13 A).[149] An interesting 1D hetero-

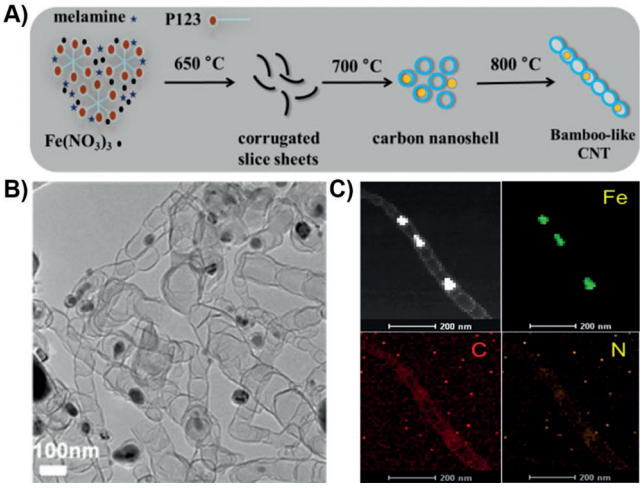

Figure 13. A) Illustration of the formation of the bamboo-like CNT/Fe_3C NP hybrids. B) TEM images and C) HAADF-STEM mapping images of the resultant catalyst. Adapted from Ref. [149].

structured nanoelectrocatalysts with Fe_3C NPs encapsulated in bamboo-like CNTs was obtained (Figure 13 B,C). The bamboo-like CNT structure is beneficial for ORR catalysis by offering more graphitic edges and thus introducing more active sites. The internal Fe_3C NPs further increase the activity of the surrounding CNT, possibly by introducing the change in the local work function of the CNT walls. As a result, the CNT/Fe_3C NPs show a higher ORR activity in alkaline media and comparable ORR onset potential in strong acidic media than Pt/C catalyst. The stability of our catalysts is much better than that of Pt/C in both solutions. Detailed investigation shows that the addition of P123 is critical to forming such well-defined nanostructures. It assists the growth of carbon into CNTs by catalytically linking rolled carbon nanosheets during the pyrolysis process (Figure 13 A). Other soft templates such as Pluronic F127, were also found to work similarly to P123 in directing the bamboo-like CNT growth.

Template-free synthesis of M-N-C catalysts with optimal nanostructures is another promising route. Owing to the lack of assistance from additional templates, a fine control over the precursor architecture is critical to obtain the desired nanostructures. As mentioned previously, $M-N_4$ macrocycle mol-

ecules were the very first and extensively studied candidate for M-N-C catalysts. The performance from pure pyrolyzed M-N_4 macrocycles was far from that of Pt-based catalysts, and correlated with their uncontrolled agglomeration. Structure control over materials derived from them can be fulfilled by constructing crosslinked or extended conjugated skeletons with high surface area and rich porosity from M-N_4 monomers by a Yamamoto reaction.[147,150] The pyrolyzed products, with well-defined 2D or 3D structures, show good catalytic activity and stability in both acidic and alkaline media. Furthermore, similar porous skeletons with rich M-N_4 macrocyclic centers can be prepared from a broad range of simple monomers instead of M-N_4 macrocyclic oligomers by cross-linking reactions,[151] which provides a more flexible methodology to construct various porous structures and coordination environments for ORR study.

5.3. Metal–Organic Frameworks ORR catalysts

Based on the above information, it is highly desirable to fabricate M-N-C precursors with a greater catalytic-site density together with a higher surface area and a richer porosity that ensures the greatest exposure of the active sites in the ORR catalyst. A new route to construct such precursors based on bottom-up synthesis is favorable. Metal–organic frameworks (MOFs), built from selected metal–ligand coordination (Figure 14), represent a highly promising candidate. MOFs featuring defined and tunable structures at a molecular level have unique properties, including high surface area, rich porosity, as well as tunable pore size and functionality.[152,153] Traditionally, they have been studied for gas storage/separation, catalysis, magnetic materials, and luminescence.[154] Recently, there is a rapidly growing interest in utilizing MOFs or their derived nanostructures for electrochemical energy storage and conversion,[155] including ORR catalysis.

The application of MOFs for ORR catalysis can be categorized into mainly three routes as depicted in Figure 14. Firstly, MOFs could be prepared with many Fe-N_4 or Co-N_4 coordinate moieties simply from the choice of metal ions and organic linkers.[159,160] After carbonization, they can be converted into ORR active materials with potentially abundant M-N-C active sites. It is estimated that the density of Co-N_4 site in a single cobalt imidazolate (CoIM) MOF crystal reaches as high as 3.6×10^{21} cm^{-3}, which ultimately leads to sufficient and uniformly distributed catalytic sites in the catalyst derived from it.[160] Moreover, the metal center in MOF skeletons can be converted into other ORR active forms, such as metal oxides (MO), metal sulfides (MS), single-metal carbides (MC), or heterometallic carbides, by changing the MOF composition or carbonization process.[80,161–163] Secondly, MOFs can be converted into metal-free ORR catalysts, such as nitrogen-doped carbons, after removal of metal species by acid etching or metal evaporation. Zn-based MOFs (e.g. ZIF-8) are the typically used MOFs. The nitrogen-rich ligands in these MOFs decompose to produce nitrogen-doped carbon during heat activation while the Zn ions are reduced into Zn metal that would vaporize owing to its low boiling point (908 °C), leaving behind highly porous

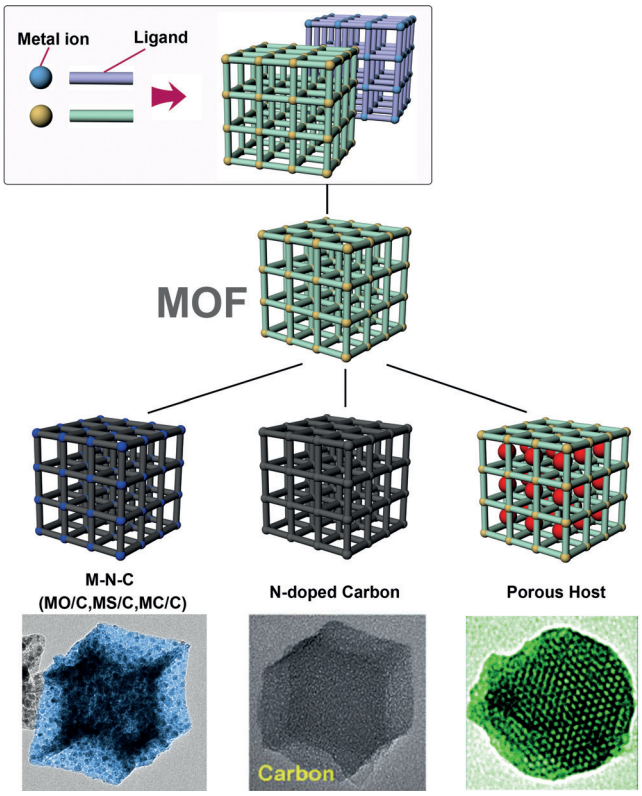

Figure 14. Schematic illustration showing the construction of a MOF-derived ORR catalyst. The TEM images are adapted from Ref. [156–158] with permissions from the Royal Society of Chemistry and Wiley-VCH.

carbon.[164,165] A variety of heteroatom dopants (e.g. N, P, or S) into the catalytic carbons can be realized by initial modification of the organic ligands or introduction of a second precursor into the pores of MOFs, which leads to various ORR catalytic behaviors.[166–168] Thirdly, MOFs can act as a microporous host for additional metal–nitrogen precursors to generate more active M-N-C catalysts as the catalytic sites are suggested only to occur in micropores.[139,169] Ferrous acetate and phenanthroline loaded ZIF-8 was prepared and converted into ORR electrocatalysts with increased activity and enhanced mass-transport properties. The catalyst delivers the highest volumetric ORR activity of 230 $A\,cm^{-3}$ at 0.8 V for non-Pt-group-metal catalysts.[14]

Furthermore, the catalytic activity of MOF-derived materials can be further enhanced from nanostructuring. MOF nano/microcrystals, nanofibers, nanowire arrays were introduced to generate ORR catalysts with more exposed active sites and better mass-transport and thus better catalytic activity.[156,170,171]

To conclude the combination of a vast choice of metal ions/ligands and tuning of the nanostructure enables a considerable flexibility in designing desired MOFs for advanced ORR catalysts. It is of great convenience to elucidate the correlation between structure, composition, and ORR performance of the MOF-based catalytic systems, which is fundamentally important for the understanding of active sites in related catalysts.

6. Metal-Free Catalysts for ORR

6.1. Porous Carbon Nanostructure

Carbon is at the heart of potentially applicable earth-abundant materials for electrochemical energy conversion and storage applications (ECSAs) owing to excellent stability, tailorable porosity, higher surface areas, and excellent electronic conductivity.[172] In ECSAs, the porosity (pore connectivity, length, and pore size distribution) is the key factor since it directly affects the mass-transfer properties and diffusion distances. Carbon materials can have variable porosities from micropores (responsible for high surface area), mesopores (suitable for active materials fabrication), to macropores (providing ease of diffusion/mass transfer).[173] In the search for highly active electrode materials, the hierarchical porous (integrated micro-/meso-/macropores) network can address various issues related from active material fabrication to mass-transfer capability. However, carbon lacks sufficient activity because of the absence of active sites, and thus needs modifications to its surface charge distributions to improve the localized interaction between carbon and adsorbed species. Chemical modifications (introduction of heteroatoms for example, N, B, S and P) have been identified to effectively improve the inherent structure (bonding, porosity, surface area, functional groups, etc.) and electronic and geometric properties of the carbon.[6] Such modifications lead to several activated points where effective adsorption and catalysis can happen. For example, introduction of N into the carbon sheets shows highly enhanced ORR performance since the N atom has a similar nuclear size to the C atom, and can provide an extra electron to the electronic cloud. Furthermore, the addition of N makes the carbon more disordered resulting in more defect sites, acting as potential sites for catalysis. The N-doped porous carbon can be synthesized by 1) direct carbonization of N-containing precursors, 2) heat treatment of carbon-containing precursors in an NH_3 atmosphere, 3) template-directed synthesis by addition of carbon and N precursors into silica templates, and 4) ionic-liquid-mediated synthesis.[174–178] Among these methods, ammonia treatment has been used widely to derive high surface area micro-/mesoporous carbons with excellent onset potential for ORR. Owing to the improved electrocatalytic properties upon N doping, subsequent increase in N concentrations generally improves the ORR performance.[179] However, the doped N may not necessarily affect the performance since the position of N directly affects the charge density. The influence of N species on ORR activity was investigated, revealing that quaternary N centers (to some extent pyridinic and pyrrolic) are responsible for the improved ORR activity of N-doped carbons.[180,181] Hence, in addition to the N content, tailoring the position of N in the carbon matrix is very critical for creating a high-performance ORR catalyst. Furthermore, tailoring carbon with a large number of edge sites and N (or other heteroatoms) doping sites is demonstrated to be an excellent way for achieving better ORR electrocatalysts.[182] Besides N, other heteroatoms (P, S, B, F, etc.) have also been doped separately into carbon or in co-doped nanostructures.[183–186] The S-doped mesoporous carbons were found to exhibit excellent stability and good activity since S also introduces electropositive centers, and further acts as activation sites for ORR.[187]

Doping of carbon with two or more heteroatoms (co-doping) has also been identified to improve the ORR performance. Interestingly, simultaneous doping of S and N significantly improves the ORR performance,[188] in which the highest ORR performance can be obtained on S,N co-doped carbon with an Fe mediator in both acidic and basic electrolytes with onset potentials significantly higher than for Pt/C. Furthermore, ternary doping of carbon was also investigated recently. The result shows a ternary doped (N-, O-, and S-) carbon catalyst, prepared by polymerization of pyrrole with $(NH_4)_2S_2O_8$ oxidant using a template method and subsequent carbonization, can display a high onset and half wave potentials of 0.96 V and 0.74 V vs. RHE, respectively, which is better than those of N,O binary doped ones.[189,190] Furthermore, it was also shown that co-doped catalysts exhibit higher performance as a result of enhanced synergistic effects in the electrocatalytic performance in comparison to mono-doped carbon.[186]

Nanostructuring of heteroatom-doped carbon is another important way to further improve the ORR activity. For instance, mesoporous carbon spheres with high surface area of approximately 350 m^2g^{-1} and large pores (ca. 16 nm) were synthesized using a copolymer (Figure 15 A),[191] showing an

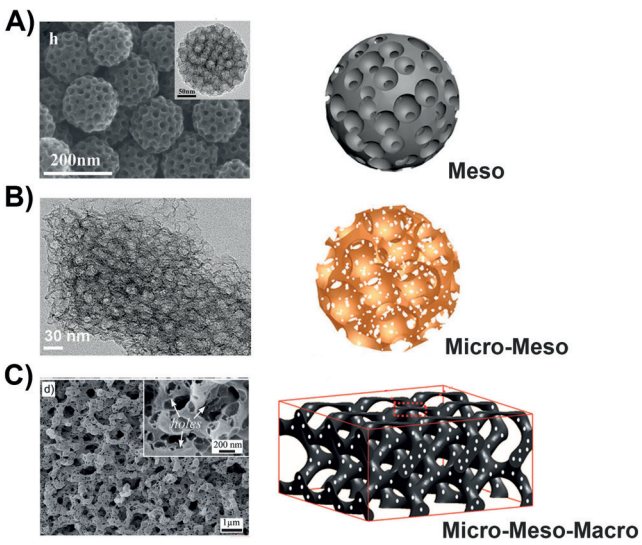

Figure 15. A) SEM image and structure model of N-doped mesoporous carbon nanospheres. Inset: TEM image. Adapted from Ref. [191] with permission by the Wiley-VCH. B) TEM image and structure model of N-doped micro/mesoporous nanocarbon. Adapted from Ref. [192] with permission from the Nature Publishing Group. C) SEM image and structure model of N-doped 3D hierarchically porous nanocarbon with micro-, meso- and macropores. Adapted from Ref. [175] with permission from Wiley-VCH.

onset potential of −0.11 V vs. Ag/AgCl, only 0.04 V less than that of Pt/C. Further elucidation of the pore size effect on ORR activity was explored, showing that both ORR kinetics and activity are largely dependent on the pore size distribution.[177,192] As shown in Figure 15 B, a hierarchical micro- and

meso-porous catalyst structure was suggested to benefit the ORR activity most. Considering the better mass diffusion in macropores and their function as an electrolyte reservoir, nanostructuring of 3D hierarchically porous carbon with micro-, meso-, and macro-porosity architecture can further improve the inherent properties of porosity, active surface, and mass transport (Figure 15C). Such a concept was demonstrated in the synthesis of N-doped 3D carbon with hierarchical pores which boosted the ORR activity, resulting in a half-wave potential of −0.133 V vs. Ag/AgCl and limiting current density of 4.54 mA cm^{-2}, values close to those of Pt/C (−0.128 V and 4.66 mA cm^{-2}, respectively).[175]

6.2. Carbon Nanotube

Since they were discovered in 1991 by Lijima,[193] carbon nanotubes (CNTs) have been investigated intensively owing to their excellent electrical and mechanical properties and wide applications from energy conversion to storage and molecular sensing.[194,195] The inherent structure of CNTs is inert and lacks sufficient activity therefore it needs further modifications to introduce activation/defect sites where catalysis can happen.[194] Introduction of oxygenated functional groups has been well documented but it was not until very recent that effect of these groups on ORR was tested.[196] It is the replacement of a carbon atom with another atom that can disturb the electronic cloud and the electroneutrality of CNTs, and thus result in enhanced catalytic properties. The electronic structure of pristine and N-doped CNTs has been studied by using density functional theory (DFT) and an improved performance for N-doped CNTs can be predicted.[195] The heteroatom doping further improves the adsorption of O_2 on the catalysts surface, favoring the Yeager model (bridge model) over Pauling model (end-on model).[197] The N-doped CNTs also show improved conductivity owing to the presence of electronegative N species which not only induce an impurity but also decrease the band gap (the Fermi level is shifted towards conduction band).[198] Vertically aligned arrays of N-doped CNTs exhibit high catalytic ORR activity, where the half-wave potential is comparable to that of Pt/C catalyst.[199,200]

Similar to N doping, other heteroatoms (P, S, and B, etc.) have also been used separately to improve the inherent structure of CNTs and enhancing ORR performance.[201–203] More recently, co-doping of CNTs with more than one heteroatom has been identified to improve the catalytic performance more effectively. However, co-doping is also accompanied by several challenging issues. For instance, in B- and N- co-doped carbon, N acts as an electron donor while B acts as an electron-accepting center affecting the overall structural dynamics. When N is doped individually, carbon atoms adjacent to the N atoms gain a positive charge and then acts as ORR center. However, B is electron deficient and when doped in carbon, B itself acts as positive center for ORR. If B- and N- bond together (B-N) in co-doped carbon, no net charge appears on the CNT for catalysis. However, if doped separately, B and N can provide their individual effects to tune the electronic structure of CNTs, providing more catalytic sites for ORR. Therefore, carefully controlling the co-doping process is the key to further improve the ORR performance over that of uncontrolled co-doped CNTs.[204]

The control on heteroatom doping is not limited to the selection of dopants; a controlled doping of the target position is also important to achieve the highest catalysis efficiency. CNTs has a unique 1D structure with outer and inner surfaces. Normally, heteroatom dopants distribute over the entire structure. However, heteroatom dopants on or near the inner surface of CNTs are hardly accessible and may not express their catalytic property. Recently, a CNT platform (CNT@NCNT) with full exposed dopants at the outer surface was introduced as an advanced nanocatalyst for ORR (Figure 16A).[205] This structure is fabricated by chemical vapor deposition (CVD) growth of N-doped carbon layers on the outer wall of pristine CNTs. TEM images show that

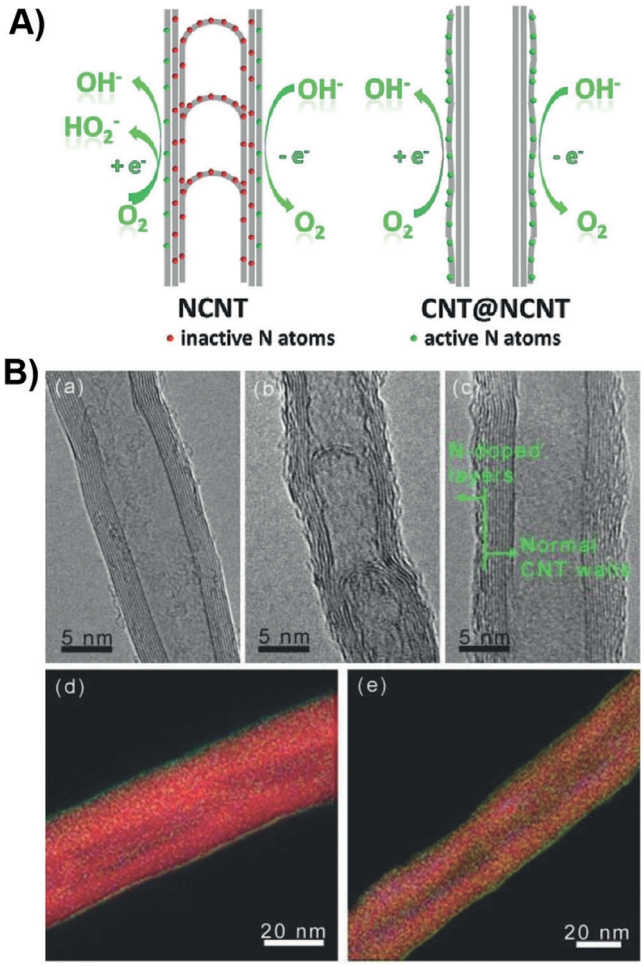

Figure 16. A) Scheme for the full exposure of 'active sites' on the surface: NCNTs with bulk doping of nitrogen atoms, and CNT@NCNT coaxial nanocables with a surface-enriched with nitrogen atoms for OER and ORR. B) Structure of a CNT@NCNT electrocatalyst with a nitrogen enriched surface: TEM images of a) pristine CNTs, b) NCNTs, and c) CNT@NCNT coaxial nanocables; element mapping showing the distribution of N (green), C (red), and O (blue), of CNT@NCNT coaxial nano-cables with the surface N/C ratio of d) 0.0238 and e) 0.0809. Adapted from Ref. [205] with permission from Wiley-VCH.

CNT@NCNT is composed of cylindrical CNT inner walls and wrinkled outer layers that are similar to pristine CNT and nitrogen-doped CNT, respectively. Energy filtered transmission electron microscopy (EFTEM) results confirm the concentrated N distribution on the outer surface of CNT@NCNT nanocable (Figure 16B). The N-doped layer can also be modulated from one to several dozen by controlling the growth duration. The optimized CNT@NCNT with an approximately 1 nm thick N-doped carbon layer affords a high onset potential of −0.015 V versus the saturated calomel electrode (SCE), which was about 58 mV more positive than that of the bulk N-doped CNTs.

6.3. Graphene

Graphene is another form of carbon with sp^2 hybridization widely studied in the last decade because of its excellent stability, electronic conductivity, and high surface area of around 2630 m^2g^{-1}.[206] Similar to CNTs, pristine graphene has limited catalytic activity that can be improved substantially by the introduction of defects or functional groups. Furthermore, substituting graphene with heteroatoms (B, P, N, S, F, etc.) has also been identified as an important approach to improve the spin and charge density of the graphene surface.[207–210] Several methods have been used to dope graphene with these heteroatoms, including CVD, ball milling, thermal annealing, and wet chemical methods.[211]

The presence of edges in the graphitic plane is suggested to be important for ORR because edges offer maximum exposure to the catalytic sites.[182] Graphene offers more edges than CNTs do, and they can be readily tailored with functional groups (e.g. H, COOH, SO_3H, COOH/SO_3H) or heteroatoms.

Synthesis of graphene with large number of edge sites has been accomplished by using ball milling and wet chemistry methods. An interesting approach to tailor the edges is using the wet chemistry to selectively improve the catalytic performance. Very recently, Friedel–Crafts acylation has been used successfully to introduce the N atoms at the edges of graphene.[212] Another easy way to introduce the heteroatom functionality at the edges is using ball milling method. Simple ball milling can be used to produce large-scale graphene functionalized with various groups (e.g. H, COOH, SO_3H, COOH/SO_3H) at selected edge sites.[213] The ORR results show graphene functionalized with -SO_3H groups provides the highest performance. Similarly, selective doping of edge sites with sulfur has also been achieved recently by using a simple dry ball milling of graphite with S_8.[214] Note that S_8-graphene does not show any considerable enhancement because attachment of S_8 cannot improve the local electronic structure of the graphene. However, S-doped into graphene induces charges that create the active centers for enhanced ORR performance. This has been further demonstrated by recent interesting examples on the reuse of S-doped graphene, produced from lithium–sulfur batteries, for enhancing ORR.[215]

However, one of the big problems in the use of heteroatom-doped graphene is that its stacking on the electrode hinders the active surface from making contact with the electrolyte, suppressing the catalytic performance. To solve this issue, the development of 3D hierarchical doped graphene-based nanostructures have also been under consideration because they offer advantages including interconnected networks, high mass transfer capability, and fully exposed active sites.[216] A more detailed study in this regard came to surface with the development of the 3D graphene nanomesh foam (GMF) for ORR catalysis.[217] As shown in Figure 17A, N-doped GMF (N-GMF) can be fabricated by

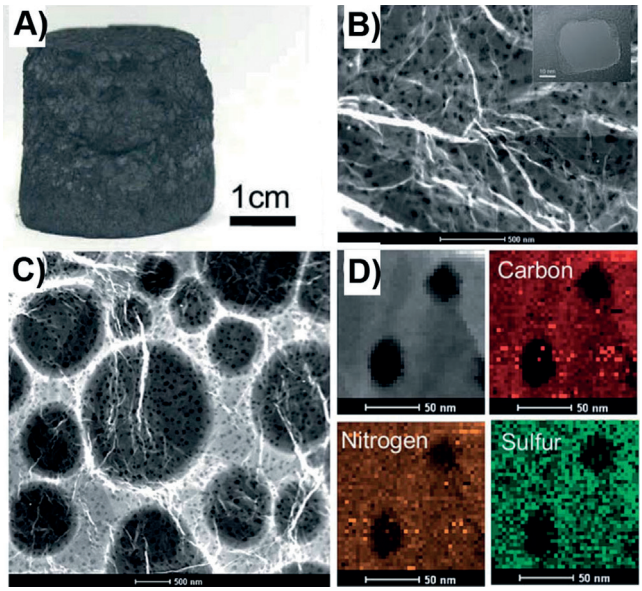

Figure 17. A) Photograph of N-GMF. B) STEM image of an individual sheet within N-GMF. C) STEM image of the sheets within the N-S-GMF. D) STEM mapping of the N-S-co-doped graphene mesh. Adapted from Ref. [217] with permission from the Royal Society of Chemistry.

first pyrolyzing the graphene/polypyrrole (polymerization of pyrrole monomer under $FeCl_3$ catalysis) composite at 850 °C and then by removing the in situ generated Fe_2O_3 NPs on N-doped graphene that can etch the graphene basal planes. Scanning transmission electron microscopy (STEM) image (Figure 17B) reveals the uniformly distributed in-plane nanopores (ca. 2–50 nm) with a high density of nearly 5.0×10^9 holes per cm^2 in N-GMF. N, S-co-doped GMF (N-S-GMF) can also be prepared by adding sulfur powder to the precursor of N-GMF before heat treatment, the porous structure is retained (Figure 17C). Elemental mappings confirm the uniform distribution of N and S dopants over the graphene mesh (Figure 17D). The developed N-S-GMF shows excellent ORR activity with an onset potential of 0.04 V (vs. Ag/AgCl), comparable to commercial Pt/C catalyst.

In essence, graphene is a "wonder material" and can contribute to higher performances in electrode materials for ORR through selective doping and tailoring of its porosity.

7. Inorganic Nanoparticle/Carbon and Carbon/Carbon Systems as Advanced ORR Catalysts

7.1. Coupled Inorganic Nanoparticle/Carbon Systems

As described in previous Sections, transition-metal-based inorganic NPs have intrinsic ORR catalytic activity, however suffer from poor electrical conductivity. Conventionally, they are loaded on electrical-conducting carbon black to display their ORR activity. The discovery of new carbon nanomaterials (e.g. N-doped CNT and graphene) that have not only high electrical conductivity but also considerable ORR activity, suggested that it should be feasible to couple ORR active inorganic NPs to the advanced carbon nanomaterials to further improve their activities. This idea is well demonstrated by the coupling of Co_3O_4 NPs with N-doped graphene, the coupled material displayed much improved ORR activity compared with the unloaded Co_3O_4 NPs and the graphene support.[87] Along this line, numerous inorganic NPs (e.g. Mn_3O_4, Fe_3O_4, $Co_{1-x}S$) were deposited on advanced carbon nanomaterials to improve their ORR activities.[93,101,130]

Owing to the distinct atom arrangements, it is not easy to incorporate inorganic NPs (e.g. metal oxides or metal sulfide) into sp^2-hybridized plane of the carbon substrates. In an inorganic NPs/carbon coupled system, the NP component is usually attached to the surface of the carbon substrates. However, the physically mixing the two components only leads to limited interactions between them, resulting in low ORR activity and stability. To ensure an intimate interaction, chemical modification on the surface of inorganic NPs or/and carbon is needed if no intrinsic interaction exists. Figure 18 summarizes the ex situ and in situ strategies to create nanocarbon hybridization that may afford strong coupling.[218] In the ex situ route, the two components are first modified with functional groups or molecular linkers and then combined under covalent or non-covalent interaction. In the in situ method, target NPs were synthesized in the presence of carbon substrates, often at the defect sites of the carbon. The structure of the NPs is usually affected by the carbon substrates as a result of the strong interaction.

The nucleation of NPs on graphene is assisted mainly by metal-ion sorption on the surface functional groups of graphene oxide. Nevertheless, the weak sorption cannot overcome the incompatibility between the NPs and graphene sheet, which may lead to less control of the morphology, particle size and NPs–graphene interactions. This issue can be settled by the solution-phase self-assembly method described for the preparation of graphene-Co/CoO NPs.[79] To prepare this hybrid system, monodisperse Co/CoO core/shell NPs were first synthesized by controlled oxidation of pre-prepared Co NPs (Figure 19A), and then assembled on the graphene surface. TEM images show that the monodisperse Co/CoO NPs were uniformly distributed on graphene (Figure 19B). ORR test shows that the graphene–Co/CoO NPs has a more positive half-wave potential (−0.176 V vs. Ag/AgCl) than Co/CoO NPs supported on conventional carbon (−0.290 V), and much more positive than the pure graphene support (Figure 19C), indicating a stronger interaction between NPs and graphene and a better ORR enhancement from graphene coupling than conventional carbon support. Figure 19D shows that the activity of the graphene-Co/CoO composite is also comparable to commercial C-Pt, making it a good candidate for ORR catalysis.

To further strengthen the interaction between NPs and carbon support, recently, we demonstrated a MOF-derived route for strongly coupling metal oxide NPs with porous carbon.[80] Traditionally, the catalysts prepared from pure MOF are rather large and dense particles in which most of the ORR-active Co@Co_3O_4 NPs are deeply embedded and lost contact with the ORR-related species. However, the catalyst from CMK-3 (a typical ordered mesoporous carbon) coupled MOF precursors has fully exposed active sites and 3D ordered open space that enables more rapid mass transport (Figure 20A). To construct this nanostructure, a Co-based MOF (ZIF-9) shell is grown on the modified CMK-3, followed by heat treatment under Ar and mild oxidation in air, giving Co@Co_3O_4@C core@bishell NPs encapsulated into a 3D highly ordered carbon matrix (Figure 20B). The graphene sheet-like carbon shells (Figure 20C), generated from the decomposed organic ligands of ZIF-9, create a very strong interaction/contact between the inner Co@Co_3O_4 NPs and the CMK-3 supports, which is critical for electron transfer between NPs and CMK-3 (enhancing the ORR activity) and preventing NPs detaching from CMK-3 (enhancing the ORR stability). As a result, the obtained catalyst displays much higher ORR activity than that of the catalyst prepared from the MOF alone. The activity displayed resembles that of commercial Pt/C catalyst in alkaline medium.

CNTs are another important class of carbon nanomaterials for coupling the active NPs to enhance ORR. However, owing to their unique 1D structure with open channel, the effective coupling of CNTs with NPs is very difficult. Recent efforts have been devoted to developing new strategies for linking NPs into/onto CNTs in different forms. Figure 21 shows the models and TEM images of CNTs/NPs. Three main patterns exist, namely, on the outer shells of CNT, inside the CNT channel, and at the CNT tips. On the outer shells is the most observed pattern as a result of its simplicity (Figure 21A), where the outer CNT surface is first activated by oxidation. The catalytic NPs are fully exposed in this case, showing a high density of active sites and excellent mass transport. All these features, put together, may lead to a better ORR performance in the resultant coupled system than that of graphene-based couple systems.[85] However, the stability of most inorganic NPs on the outer surface is not good, particularly in acidic media. For the second pattern, NPs inside the CNT channel, Fe NPs were encapsulated into the compartments of pod-like CNTs via a simple one-step heat treatment of ferrocene and sodium azide precursors at 350 °C.[219] Fe NPs outside the CNTs were removed by acid etching. The remaining Fe NPs were completely isolated in the compartments of the CNTs (Figure 21B). Bare Fe NPs are susceptible to O_2 and SO_2, and can be easily poisoned by CN^- ions, leading to poorer ORR activity. In comparison, the Fe NPs in the CNT were well shielded by CNT walls against these species leading to a stable performance as ORR catalyst. Since these Fe NPs were not in direct contact with electrolyte, they were suggested to contribute to the ORR

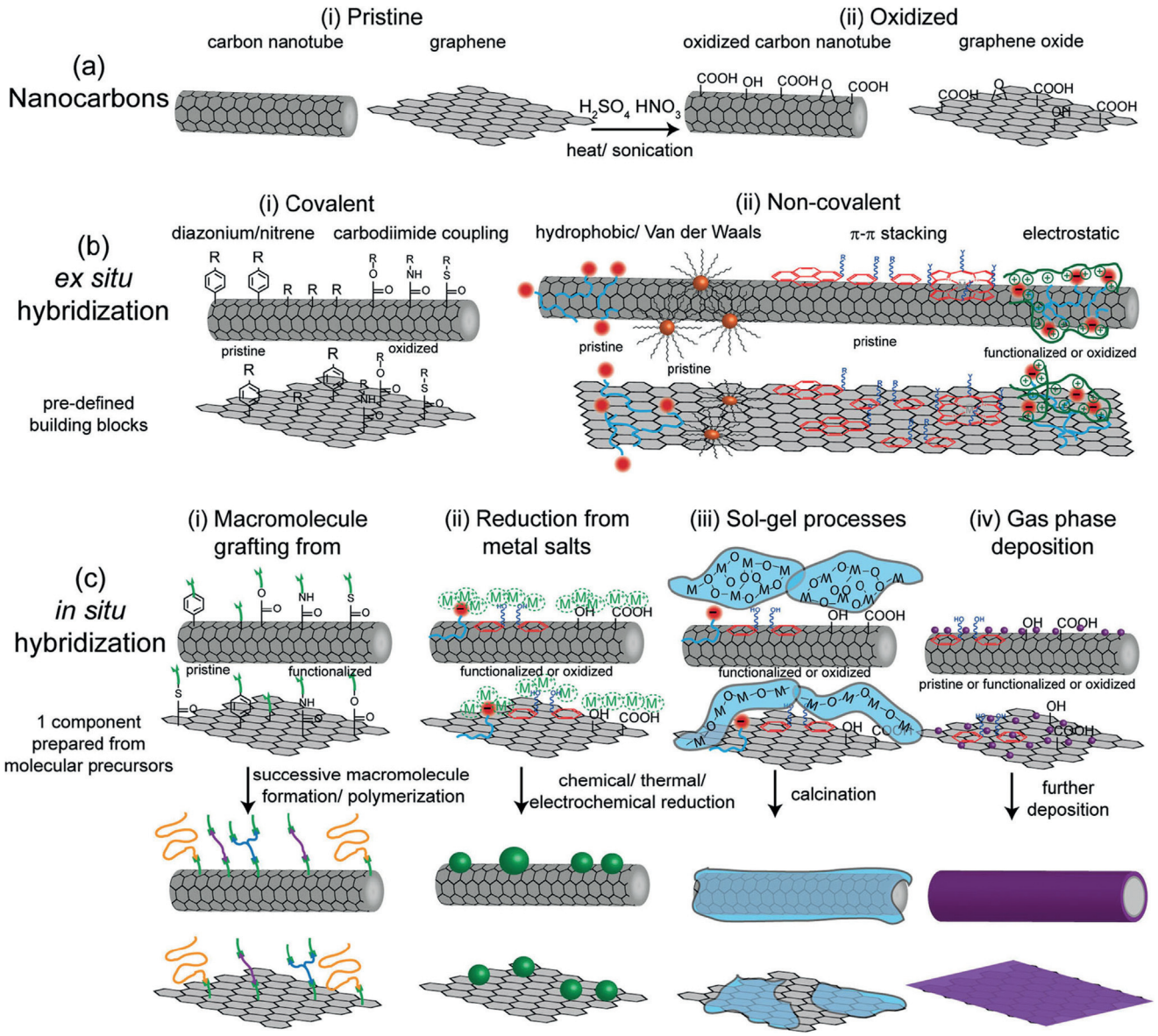

Figure 18. Summary of nanocarbon hybridization strategies. a) The chosen strategy depends upon nature of nanocarbon which can be either i) pristine or ii) oxidized; b) ex situ synthesis of nanocarbon hybrids from predefined building blocks can be completed via a range of i) covalent and ii) non-covalent techniques, both for pristine and oxidized (as highlighted by oxygen functional groups in the Figure); c) in situ synthesis of the hybrid component in presence of the nanocarbon can be achieved following various strategies depending upon the second component including: i) grafting from for polymers and macromolecules, ii) chemical reduction for metallic or semiconducting NPs, iii) sol-gel processes for semiconducting thin films or NPs and iv) gas-phase deposition for thin metallic or semiconducting films; in situ hybridization is improved when there is an attractive interaction between precursor and nanocarbon, which is typically achieved via oxidation (as highlighted by oxygen functional groups in the Figure) or non-covalent functionalization of pristine nanocarbons (such as in (b) (ii). Adapted from Ref. [218] with permission from Wiley-VCH.

activity by decreasing the local work function of the CNT surface. Partially embedding NPs at CNT tips is the third pattern that can also afford intimate contact between the NPs and CNTs (Figure 21 C). Meanwhile, in the system where these NPs are stable (e.g. metal oxides in alkaline solution) the NPs are able to participate directly in ORR catalysis, which may lead to improved catalytic activity. Building such a sophisticated structure is based on the initial formation of NPs-in-CNTs followed by oxidative thermal scission that can rupture the CNTs and oxidize the residual NPs concurrently (Figure 21 B). Through this method, spinel Mn-Co oxides at the tips of N-doped CNT were successfully prepared, which demonstrated the impressive activity for both ORR and oxygen evolution.[220]

7.2. Coupled Carbon/Carbon Nanomaterials

Coupled Carbon/carbon nanostructures are feasible for enhancing ORR because the better compatibility between the

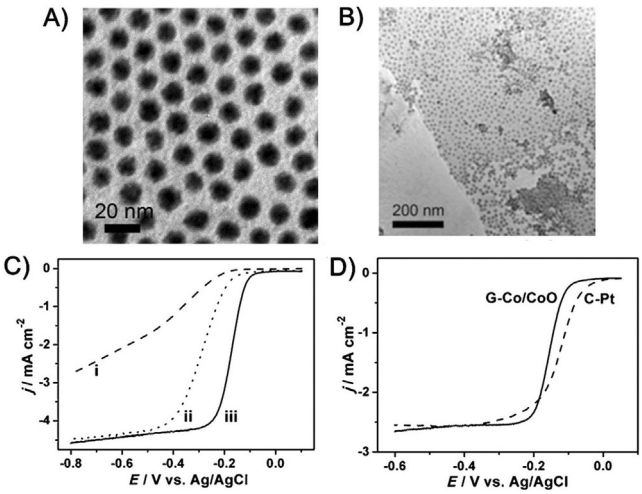

Figure 19. TEM images of A) Co/CoO and B) grapheme (G)-Co/CoO NPs. C) ORR polarization curves of i) graphene, ii) C-Co/CoO, and iii) G-Co/CoO NPs. D) ORR polarization curves of G-Co/CoO NPs and the commercial C-Pt catalyst. Adapted from Ref. [79]

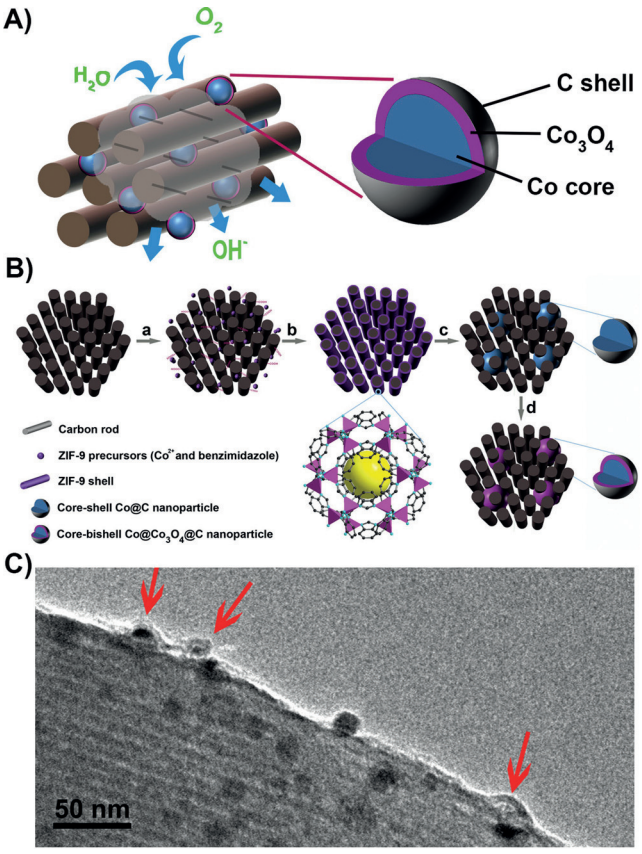

Figure 20. A) Structure model of $Co@Co_3O_4@C$ core@bishell NPs encapsulated into 3D highly ordered carbon matrix for promoting the ORR. B) SEM and C),D) TEM images of $Co@Co_3O_4@C$ core@bishell NPs encapsulated into 3D highly ordered carbon matrix. Arrows in (C) show the graphene sheet-like porous carbon shells. Adapted from Ref. [80] with permission from the Royal Society of Chemistry.

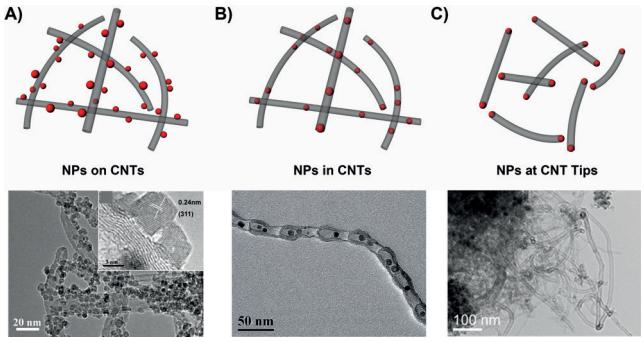

Figure 21. Model and micrographs of metal NPs/CNT nanosturctures: A) CoO NPs anchored on the surface of CNTs; B) Fe NPs inside the CNTs, and C) spinel Mn-Co oxide NPs at the CNT tips. Micrograph in (A) reprinted from Ref. [85] with permission from the American Chemical Society. Micrograph in (B) reprinted from Ref. [219] with permission from Wiley-VCH. Micrograph in (C) reprinted from Ref. [220] with permission from American Chemical Society.

ORR-active carbon nanomaterials and the carbon substrates can principally reduce the interface resistance, leading to a faster electron transfer from the conducting carbon substrates to the supported catalytic carbon unit and ultimately to the adsorbed oxygen molecules. Inspired by this, a number of coupled carbon/carbon nanostructures have been developed. Typical examples include graphene quantum dots, N-doped porous carbons, carbon nitrides, CNTs, carbon nanofibers coupled with 1D (e.g. CNT, carbon nanofiber), 2D (e.g. graphene), or 3D substrates (e.g. CMK-3).[221–228]

Despite the tremendous efforts, achieving seamless connection between the subunits in these coupled systems remains a huge challenge. Instead of physical mixing the as-formed subunits, it is more feasible to construct the ORR-active component in the presence of or from the carbon substrate, which may generate a stronger physical or chemical connection. Few-walled CNTs have been chosen for such investigations.[200] They were treated in a $KMnO_4/H_2SO_4$ mixture at 65 °C. Under such harsh oxidation conditions, the outer walls of the CNTs were partially unzipped, forming graphene oxide pieces and nanoribbons that were firmly attached to the intact inner tubes. Under a subsequent NH_3 activation, the defect- and edge-rich graphene units were converted into highly active N-doped graphene while keeping the seamless contact with the inner conducting tubes. As a result, the CNT-graphene complexes obtained exhibit a high ORR activity and stability in acidic media together with a Pt-like ORR activity in alkaline media.

Simultaneous growth of the ORR-active carbon unit and the conducting carbon structure is an important and efficient method to ensure covalent C–C bonding between the subunits in coupled systems. CNTs with end coupling to N-doped graphene via a C–C bond were prepared by a one-step CVD growth.[229] FeMoMgAl layered double hydroxides (LDHs) were used as a bifunctional catalyst for graphene and CNT formation under a methane flow as the carbon source. The graphene/CNT complexes obtained have a 3D interconnected network, which can avoid the entanglement or stacking that often happens in 1D and 2D carbon nano-

structures, leading to improved mass diffusion. Considering the influence of the overall structure on the ORR activity, a possible ideal coupled system would be the "vein-leaf" type 3D porous network consisting of hard and electrical conducting carbon nanofibers or nanotubes as the backbones and an ORR active nanosheet as the flexible leaf. It can facilitate the required rapid electron transfer and mass diffusion for ORR (Figure 22 A,B). The advanced structure has been realized recently by a simple calcination of the mixture of two cheap and abundant biomasses, bacterial cellulose (BC) and urea.[230] The chosen BC pellicles have an intrinsic 3D interconnected scaffold (Figure 22 C) and were converted into the carbon nanofiber backbones after carbonization, while urea was used as the precursor to generate layered graphitic carbon nitride (g-C_3N_4) in the interlayer voids (Figure 22 D). As the reaction proceeds, the carbon intermediates from BC gradually diffuse into the adjacent g-C_3N_4 and are ultimately condensed into N-doped graphene, affording a covalent C–C bonded graphene/carbon nanofiber coupled system (Figure 22 E,F). Compared with the CVD growth, this method seems to be much easier and more cost effective. Along with the good ORR activity and stability, it can be a good choice as a Pt alternative.

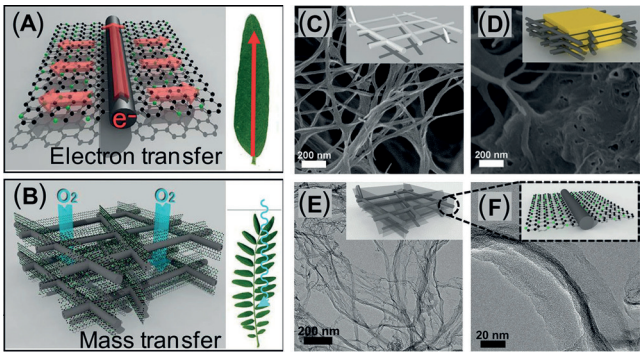

Figure 22. A) CNF@NG "vein-leaf" structure for enhancing electron transfer. (Carbon atoms are black or gray and nitrogen atoms are green). B) The complex interpenetrated 3D network structure of CNF@NG, facilitating mass transfer (exemplified with molecular oxygen). C) The freeze-dried bacterial cellulose (BC) monolith (white rods) with an interpenetrating 3D network structure. D) The carbonized BC (CNF, black rods) wrapped by the g-C_3N_4 sacrificial template (yellow) after thermal condensation of the mixture of BC and urea at 600 °C resulting in the CNF@g-C_3N_4 hybrid. E) The CNF@NG was released after removal of g-C_3N_4 by heating at 900 °C. F) The magnified view of CNF@NG. Carbon atoms are black or gray and nitrogen atoms are green. Adapted from Ref. [230] with permission from Wiley-VCH.

8. Electrochemical Evaluation for ORR at the Microscale

The advent of advanced nanostructures presents new challenges to researchers who are trying to elucidate the correlation between catalyst structure and electrocatalytic behavior. Conventional MEA and RDE measurements work on the aggregation of catalyst NPs, only showing the average catalytic properties. While NP-based ORR catalysis is quite complicated, usually a combination of several effects, such as particle size, geometry, surface area, composition, and even the thickness and homogeneity of the final catalyst layer. Though there are some good results revealing the effects that one of these elements exerts on the ORR performance, it is hard to completely exclude the influence from other factors. For example, in studying facet-dependent ORR properties, metal NPs with well-defined facet can be obtained through the fine chemical syntheses. However, the NP size, also reported as an important factor in determining ORR activity, is unlikely to be controlled at the same level simultaneously. The situation is worse in non-precious catalyst system where the chemical composition and microstructure are more complex.

To develop better non-precious catalysts for ORR, it is essential to recognize the active centers and what structures are more beneficial. Therefore, it is of great interest and fundamental importance to focus our measurement scope on the microscale, and study an individual catalyst particle or a target position during electrochemical reaction. It can open a new world in electrocatalyst study, and help us to uncover the hidden details in the electrocatalytic process, and ultimately contribute to the design of advanced nanostructures for better ORR catalysis. The investigation of catalysis on the microscale has long been suggested in electrochemistry studies, however has been hindered by a number of challenges, such as microdetector manufacture, single NP isolation, response sensitivity, or signal-to-noise ratio.[231,232]

Transient particle–electrode collision has been reported as a useful methodology in studying the electrocatalysis at the single NP level.[233–235] It is based on a large current amplification that happens when a catalytic NP collides with the inert microelectrode surface during the reaction. By modifying the NPs, the applied potential, and the indicator concentration, a series of time-dependent Faradaic-response profiles can be obtained, allowing the study of electron-transfer kinetics at the microscale. Scanning electrochemical microscopy (SECM) is another efficient tool for electrocatalytic activity investigation on the microscale. Catalytic NPs attached on the inert electrode are scanned by the nanosized tips in the SECM during an electrochemical reaction process. The tip current is recorded as a function of *x*–*y* position or distance, offering electrochemical mapping of the target position with spatial resolution. It allows for screen analysis of separate NP arrays simultaneously[236] or the detection of individual catalytic NP.[237] The above methodologies are based on the usage of a micro- or nanoelectrode, the size of which largely determines the resolution of the test. Pt disk electrodes with radii as small as 1–3 nm have been prepared,[238] which can provide high precision in measuring ultrafast electrochemical kinetics and target-point studies. Besides the microelectrode-based techniques, optical measurements, such as surface plasmon resonance imaging[239,240] and single-molecule fluorescence imaging[241,242] have also been developed to visualize and quantitate the catalytic activity on single nanocatalysts. These techniques replace the scanning probe or the microelectrode in monitoring the

current with an optical signal probe. Surface plasmon resonance imaging, for example, measures the plasmonic signals that are generated from the bulk refractive index changes near the electrode and directly related to the electrochemical current density.[239]

Though remarkable successes in microelectrode and optical imaging based studies on nanocatalysts has been achieved, related investigations on ORR catalysts are very rare, perhaps because of the complex pathways and the subtle changes in local environment during the reaction process. Among the few reports, the SECM method stands out as an efficient way in examining the electrocatalytic activity of potential ORR catalysts.[236,243,244] Bard and co-workers[245] fabricated catalyst spots consisting of binary and ternary alloys of Pd, Au, Ag, and Co (or Cu) arranged in arrays on a glassy carbon (GC) electrode. In a standard preparation process, metal salt precursors were first deposited on the GC by a piezo-based microarray dispenser and then reduced with hydrogen. The ORR catalytic activity of each sample was examined by an SECM technique that enables rapid screen of the activity of catalysts with a wide range of compositions. Parallel experiments based on conventional RDE were in good agreement with the results from SECM, demonstrating the accuracy and convenience in the microscale measurement for ORR investigation.

Micro- or nanoelectrodes can be very useful for structure-dependent ORR investigations, particularly with regard to the non-precious catalysts, such as CNT and graphene. As described in previous Sections, heteroatom-doped CNTs can function as direct ORR catalysts, support materials, or conducting agents. However, pristine CNTs only function as conducting agents in most cases. Little attention was paid to the ORR catalytic reactivity of pristine CNTs without dopant or modification. Very recently, by using a scanning electrochemical cell microscopy (SECCM), ORR activity along individual pristine single-walled CNTs (SWNT) has been visualized.[246] Figure 23 A schematically illustrates the device for SECCM measurement. The main part of this device is a tapered theta pipet with two channels filled with electrolyte solution, which provides a dynamic electrochemical cell in the meniscus at the pipet end.[247] The substrate acts as the working electrode, and Ag/AgCl as the quasi-reference in each pipet channel functions as the counter electrode to control the potential. A potential (V_2) is applied between the two Ag/AgCl electrodes, leading to a DC current (I_{IC}). The perpendicular position of the pipet is monitored by an AC current caused by the small amplitude oscillation of the pipet. A working potential is applied on the substrate (V_1). When the meniscus comes into contact with the SWNT sample, an electrochemical current (I_{EC}) is measured using the high sensitivity current-to-voltage converter, leading to the direct electrochemical mapping of the sample. The SECCM test suggests substantial electrochemical activity in pristine SWNT for ORR and also the catalytic reactivity is correlated with the local structure. The kinked and oxidized sites in SWNT are particularly active.

Revealing the exact active sites in graphene is also of considerable interests in ORR catalysis study. The experimental investigation shows that the edges of graphene are more active toward ORR than the basal plane.[217,249] This result has been confirmed by the theoretical results, suggesting that oxygen adsorption on edge or defect spots is easier than that on the integrated basal plane.[250,251] Despite the above successes from experimental and simulation work, direct evidence that links the ORR activity obtained with these sites is still absent. The situation has changed recently with the help of microscale electrochemical evaluation.[248,252,253] A simple but very efficient micro apparatus was introduced, as shown in Figure 23 B.[248] A Pt wire and a Ag/AgCl wire were integrated into a capillary tube functioning as the counter and reference electrodes, respectively. An air-saturated electrolyte microdroplet was deposited on a highly oriented pyrolytic graphite (HOPG; the working electrode). Thus, an effective electrochemical cell was constructed when the capillary tube tip was immersed in the droplet which could be located at any specified spot on the HOPG, allowing the activity to be studied on the edge or on the basal plane. Linear-sweep voltammetry was performed on both sites, showing a more positive onset potential and higher current density on the edge than on the basal plane.

From this perspective, the microscale electrochemical evaluation is an efficient methodology for ORR catalyst study. The resulting information on structure-dependent

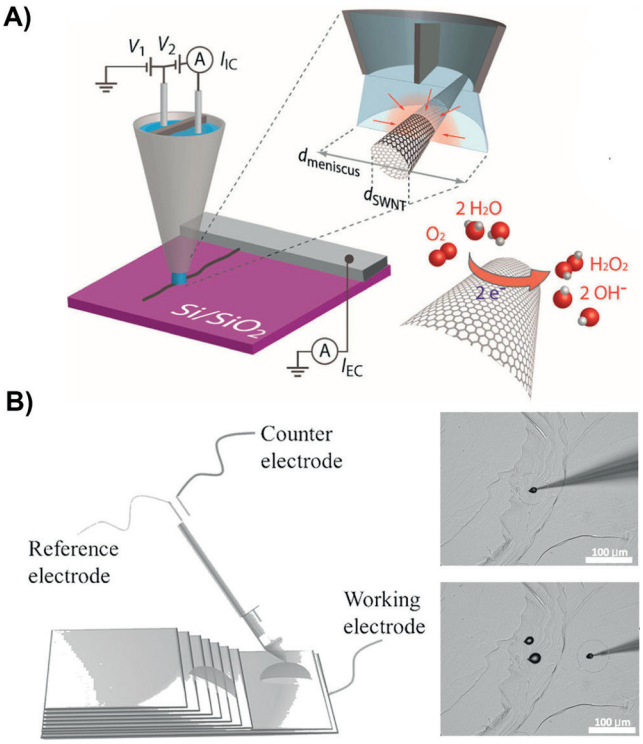

Figure 23. A) SECCM setup showing a theta pipet positioned directly above an individual SWNT creating a well-defined tiny meniscus electrochemical cell for local electrochemical measurements and substrate mapping. Adapted from Ref. [246] with permission from the American Chemical Society. B) Micro apparatus for the ORR electrochemical experiment (left). Optical photograph of the HOPG as the working electrode with the air-saturated droplet deposited either on the edge or on the basal plane of the HOPG electrode (right). Adapted from Ref. [248] with permission from Wiley-VCH.

ORR reactivity can provide general guidance for building particular architectures or microstructures for future high-performance ORR catalysts.

9. Conclusions and Outlook

Since the pioneering work reported by Jasinski in 1964, great efforts have been paid to engineering cheaper and earth-abundant nanomaterials to replace Pt for oxygen reduction catalysis. A vast range of materials, including metal oxides, metal chalcogenides, metal carbides, metal nitrides, M-N-C, and heteroatom-doped carbons, have been developed. Despite the great efforts, there is still an clear gap in the ORR activities between these materials and Pt, particularly in acidic media. To make them truly competitive, future improvement is required in:

1) the intrinsic turnover frequency per active site, as the value is commonly low when compared with that of Pt, thus more rational design of nanocatalysts with particular structures are needed to maintain the desired output.
2) the catalytic active site density, as the volumetric current density largely depend on this parameter.
3) the electron/mass transport properties, as oxygen reduction proceeds at three-phase boundaries; faster transport leads to accelerated ORR process.
4) the stability in harsh condition, as the ORR catalysts in practical utilization are normally exposed to highly oxidative and corrosive environments.

Along these lines, attempts at composition tuning and nanostructuring have been made and shown remarkable improvements in the overall ORR catalytic activity as well as the stability of the earth-abundant catalysts. Binary or ternary metal NPs are highly promising owing to their strong electronic and strain effects that are beneficial for oxygen sorption or activation. Besides the crystalline inorganic NPs, it is interesting to find that some amorphous inorganic NPs with a high density of defects and a high surface area also have promising ORR activity. The presence of unusual bonding arrangements in the amorphous catalysts may benefit the ORR activity. M-N-C type catalysts have also attracted tremendous attention. Recent efforts on constructing nanostructured M-N-C catalysts provide an exciting opportunity for ORR performance enhancement. CNTs and graphene are advanced carbon materials with high electrical conductivity and stability. They have considerable ORR activity when they are doped with some heteroatoms in the proper atomic arrangement. On the other hand, they can be used as a good electron-conducting matrix when coupled with other ORR active species. Moreover, the strong interaction between the coupled subunits may generate improved acidity and stability for ORR.

Despite the remarkable progress in earth-abundant catalysts, the nature of ORR active sites in these materials remains a debate. The development in materials synthesis and characterization may offer a good opportunity to elucidate these sites. MOFs, build from selected metal–ligand coordination, can be used as a new precursor to construct M-N-C catalysts with high active site density and rich porosity. The flexibility in designing MOFs may facilitate systematic investigation of the correlation between structure, composition, and ORR performance, thus helping to identify the active centers. Moreover, the advent of advanced techniques such as micro-/nano-electrode, scanning electrochemical cell microscopy, and optical imaging, could enable investigations at the microscale, which may provide a powerful tool for in situ monitoring of the electrochemical process at the target position with considerable spatial resolution and thus aid the rational design of ORR catalysts with optimized activity.

Acknowledgements

R.Z. acknowledges the support from National Natural Science Foundation of China (11175006, 51322205, and 21371014), the New Star Program of Beijing Committee of Science and Technology (2012004).

How to cite: *Angew. Chem. Int. Ed.* **2016**, *55*, 2650–2676
Angew. Chem. **2016**, *128*, 2698–2726

[1] J. Lee, B. Jeong, J. D. Ocon, *Curr. Appl. Phys.* **2013**, *13*, 309–321.
[2] W. Vielstich, A. Lamm, H. Gasteiger, *Handbook of Fuel Cells: Fundamentals, Technology, Applications*, Wiley, Chichester, **2003**.
[3] A. A. Gewirth, M. S. Thorum, *Inorg. Chem.* **2010**, *49*, 3557–3566.
[4] J. Larminie, A. L. Dicks, *Fuel Cell Systems Explained*, 2nd ed., Wiley, Hoboken, **2003**.
[5] H. A. Gasteiger, J. E. Panels, S. G. Yan, *J. Power Sources* **2004**, *127*, 162–171.
[6] Y. J. Wang, D. P. Wilkinson, J. Zhang, *Chem. Rev.* **2011**, *111*, 7625–7651.
[7] V. Stamenkovic, B. S. Mun, K. J. J. Mayrhofer, P. N. Ross, N. M. Markovic, J. Rossmeisl, J. Greeley, J. K. Nørskov, *Angew. Chem. Int. Ed.* **2006**, *45*, 2897–2901; *Angew. Chem.* **2006**, *118*, 2963–2967.
[8] S. Guo, S. Zhang, S. Sun, *Angew. Chem. Int. Ed.* **2013**, *52*, 8526–8544; *Angew. Chem.* **2013**, *125*, 8686–8705.
[9] Y. Bing, H. Liu, L. Zhang, D. Ghosh, J. Zhang, *Chem. Soc. Rev.* **2010**, *39*, 2184–2202.
[10] I. E. L. Stephens, A. S. Bondarenko, U. Grønbjerg, J. Rossmeisl, I. Chorkendorff, *Energy Environ. Sci.* **2012**, *5*, 6744–6762.
[11] J. Wu, H. Yang, *Acc. Chem. Res.* **2013**, *46*, 1848–1857.
[12] Y. Nie, L. Li, Z. Wei, *Chem. Soc. Rev.* **2015**, *44*, 2168–2201.
[13] Z. Chen, D. Higgins, A. Yu, L. Zhang, J. Zhang, *Energy Environ. Sci.* **2011**, *4*, 3167–3192.
[14] E. Proietti, F. Jaouen, M. Lefèvre, N. Larouche, J. Tian, J. Herranz, J.-P. Dodelet, *Nat. Commun.* **2011**, *2*, 416.
[15] V. R. Stamenkovic, B. Fowler, B. S. Mun, G. Wang, P. N. Ross, C. A. Lucas, N. M. Marković, *Science* **2007**, *315*, 493–497.
[16] M. T. Koper, *Phys. Chem. Chem. Phys.* **2013**, *15*, 1399–1407.
[17] I. Katsounaros, S. Cherevko, A. R. Zeradjanin, K. J. Mayrhofer, *Angew. Chem. Int. Ed.* **2014**, *53*, 102–121; *Angew. Chem.* **2014**, *126*, 104–124.
[18] M. T. M. Koper, *J. Electroanal. Chem.* **2011**, *660*, 254–260.
[19] E. Yeager, *Electrochim. Acta* **1984**, *29*, 1527–1537.
[20] J. K. Nørskov, J. Rossmeisl, A. Logadottir, L. Lindqvist, J. R. Kitchin, T. Bligaard, H. Jónsson, *J. Phys. Chem. B* **2004**, *108*, 17886–17892.

[21] I. Morcos, E. Yeager, *Electrochim. Acta* **1970**, *15*, 953 – 975.
[22] M.-h. Shao, P. Liu, R. R. Adzic, *J. Am. Chem. Soc.* **2006**, *128*, 7408 – 7409.
[23] A. S. Bondarenko, I. E. L. Stephens, H. A. Hansen, F. J. Pérez-Alonso, V. Tripkovic, T. P. Johansson, J. Rossmeisl, J. K. Nørskov, I. Chorkendorff, *Langmuir* **2011**, *27*, 2058 – 2066.
[24] B. Hammer, J. K. Nørskov, *Adv. Catal.* **2000**, *45*, 71 – 129.
[25] J. K. Nørskov, T. Bligaard, J. Rossmeisl, C. H. Christensen, *Nat. Chem.* **2009**, *1*, 37 – 46.
[26] Y. Jiao, Y. Zheng, M. Jaroniec, S. Z. Qiao, *J. Am. Chem. Soc.* **2014**, *136*, 4394 – 4403.
[27] X. Zhou, J. Qiao, L. Yang, J. Zhang, *Adv. Energy Mater.* **2014**, *4*, 1301523.
[28] N. Daems, X. Sheng, I. F. J. Vankelecom, P. P. Pescarmona, *J. Mater. Chem. A* **2014**, *2*, 4085 – 4110.
[29] H. A. Gasteiger, S. S. Kocha, B. Sompalli, F. T. Wagner, *Appl. Catal. B* **2005**, *56*, 9 – 35.
[30] S. Sun, C. B. Murray, D. Weller, L. Folks, A. Moser, *Science* **2000**, *287*, 1989 – 1992.
[31] K. Yamamoto, T. Imaoka, W.-J. Chun, O. Enoki, H. Katoh, M. Takenaga, A. Sonoi, *Nat. Chem.* **2009**, *1*, 397 – 402.
[32] M. Shao, A. Peles, K. Shoemaker, *Nano Lett.* **2011**, *11*, 3714 – 3719.
[33] S. Guo, S. Zhang, D. Su, S. Sun, *J. Am. Chem. Soc.* **2013**, *135*, 13879 – 13884.
[34] J. Greeley, I. E. L. Stephens, A. S. Bondarenko, T. P. Johansson, H. A. Hansen, T. F. Jaramillo, J. Rossmeisl, I. Chorkendorff, J. K. Nørskov, *Nat. Chem.* **2009**, *1*, 552 – 556.
[35] C. Wang, M. Chi, D. Li, D. Strmcnik, D. van der Vliet, G. Wang, V. Komanicky, K. C. Chang, A. P. Paulikas, D. Tripkovic, J. Pearson, K. L. More, N. M. Markovic, V. R. Stamenkovic, *J. Am. Chem. Soc.* **2011**, *133*, 14396 – 14403.
[36] D. Wang, H. L. Xin, R. Hovden, H. Wang, Y. Yu, D. A. Muller, F. J. DiSalvo, H. D. Abruña, *Nat. Mater.* **2013**, *12*, 81 – 87.
[37] S. Zhang, X. Zhang, G. Jiang, H. Zhu, S. Guo, D. Su, G. Lu, S. Sun, *J. Am. Chem. Soc.* **2014**, *136*, 7734 – 7739.
[38] Q. Li, L. Wu, G. Wu, D. Su, H. Lv, S. Zhang, W. Zhu, A. Casimir, H. Zhu, A. Mendoza-Garcia, S. Sun, *Nano Lett.* **2015**, *15*, 2468 – 2473.
[39] S. Guo, D. Li, H. Zhu, S. Zhang, N. M. Markovic, V. R. Stamenkovic, S. Sun, *Angew. Chem. Int. Ed.* **2013**, *52*, 3465 – 3468; *Angew. Chem.* **2013**, *125*, 3549 – 3552.
[40] H. Zhu, S. Zhang, S. Guo, D. Su, S. Sun, *J. Am. Chem. Soc.* **2013**, *135*, 7130 – 7133.
[41] C. Chen, Y. Kang, Z. Huo, Z. Zhu, W. Huang, H. L. Xin, J. D. Snyder, D. Li, J. A. Herron, M. Mavrikakis, M. Chi, K. L. More, Y. Li, N. M. Markovic, G. A. Somorjai, P. Yang, V. R. Stamenkovic, *Science* **2014**, *343*, 1339 – 1343.
[42] X. Huang, Z. Zhao, L. Cao, Y. Chen, E. Zhu, Z. Lin, M. Li, A. Yan, A. Zettl, Y. M. Wang, X. Duan, T. Mueller, Y. Huang, *Science* **2015**, *348*, 1230 – 1234.
[43] R. B. Levy, M. Boudart, *Science* **1973**, *181*, 547 – 549.
[44] F. Mazza, S. Trassatti, *J. Electrochem. Soc.* **1963**, *110*, 847 – 849.
[45] J. D. Voorhies, *J. Electrochem. Soc.* **1972**, *119*, 219 – 222.
[46] K. Lee, A. Ishihara, S. Mitsushima, N. Kamiya, K.-I. Ota, *Electrochim. Acta* **2004**, *49*, 3479 – 3485.
[47] R. Yang, A. Bonakdarpour, J. R. Dhan, *J. Electrochem. Soc.* **2007**, *154*, B1.
[48] D. R. McIntyre, A. Vossen, J. R. Wilde, G. T. Burstein, *J. Power Sources* **2002**, *108*, 1 – 7.
[49] M. Ferrandon, A. J. Kropf, D. J. Myers, K. Artyushkova, U. Kramm, P. Bogdanoff, G. Wu, C. M. Johnston, P. Zelenay, *J. Phys. Chem. C* **2012**, *116*, 16001 – 16013.
[50] Z. Wen, S. Ci, F. Zhang, X. Feng, S. Cui, S. Mao, S. Luo, Z. He, J. Chen, *Adv. Mater.* **2012**, *24*, 1399 – 1404.
[51] M. Xiao, J. Zhu, L. Feng, C. Liu, W. Xing, *Adv. Mater.* **2015**, *27*, 2521 – 2527.
[52] J.-S. Lee, G. S. Park, S. T. Kim, M. Liu, J. Cho, *Angew. Chem. Int. Ed.* **2013**, *52*, 1026 – 1030; *Angew. Chem.* **2013**, *125*, 1060 – 1064.
[53] J. Wang, G. Wang, S. Miao, X. Jiang, J. Li, X. Bao, *Carbon* **2014**, *75*, 381 – 389.
[54] K. Ai, Y. Liu, C. Ruan, L. Lu, G. M. Lu, *Adv. Mater.* **2013**, *25*, 998 – 1003.
[55] Y. Hu, J. O. Jensen, W. Zhang, L. N. Cleemann, W. Xing, N. J. Bjerrum, Q. Li, *Angew. Chem. Int. Ed.* **2014**, *53*, 3675 – 3679; *Angew. Chem.* **2014**, *126*, 3749 – 3753.
[56] W. Yang, Y. Zhai, X. Yue, Y. Wang, J. Jia, *Chem. Commun.* **2014**, *50*, 11151 – 11153.
[57] Y. Hu, J. O. Jensen, W. Zhang, S. Martin, R. Chenitz, C. Pan, W. Xing, N. J. Bjerrum, Q. Li, *J. Mater. Chem. A* **2015**, *3*, 1752 – 1760.
[58] C. Giordano, M. Antonietti, *Nano Today* **2011**, *6*, 366 – 380.
[59] D. J. Ham, J. S. Lee, *Energies* **2009**, *2*, 873 – 899.
[60] H. Zhong, H. Zhang, G. Liu, Y. Liang, J. Hu, B. Yi, *Electrochem. Commun.* **2006**, *8*, 707 – 712.
[61] S. Isogai, R. Ohnishi, M. Katayama, J. Kubota, D. Y. Kim, S. Noda, D. Cha, K. Takanabe, K. Domen, *Chem. Asian J.* **2012**, *7*, 286 – 289.
[62] L. Kong, Z. Ren, S. Du, J. Wu, H. Fu, *Chem. Commun.* **2014**, *50*, 4921 – 4923.
[63] B. Cao, J. C. Neuefeind, R. R. Adzic, P. G. Khalifah, *Inorg. Chem.* **2015**, *54*, 2128 – 2136.
[64] T. Huang, S. Mao, G. Zhou, Z. Wen, X. Huang, S. Ci, J. Chen, *Nanoscale* **2014**, *6*, 9608 – 9613.
[65] Y. Dong, J. Li, *Chem. Commun.* **2015**, *51*, 572 – 575.
[66] M. Lei, J. Wang, J. R. Li, Y. G. Wang, H. L. Tang, W. J. Wang, *Sci. Rep.* **2014**, *4*, 6013.
[67] T. Sun, Q. Wu, R. Che, Y. Bu, Y. Jiang, Y. Li, L. Yang, X. Wang, Z. Hu, *ACS Catal.* **2015**, *5*, 1857 – 1862.
[68] T. Ando, S. Izhar, H. Tominaga, M. Nagai, *Electrochim. Acta* **2010**, *55*, 2614 – 2621.
[69] J. Chen, K. Takanabe, R. Ohnishi, D. Lu, S. Okada, H. Hatasawa, H. Morioka, M. Antonietti, J. Kubota, K. Domen, *Chem. Commun.* **2010**, *46*, 7492 – 7494.
[70] M. Liu, Y. Dong, Y. Wu, H. Feng, J. Li, *Chem. Eur. J.* **2013**, *19*, 14781 – 14786.
[71] L. An, W. Huang, N. Zhang, X. Chen, D. Xia, *J. Mater. Chem. A* **2014**, *2*, 62 – 65.
[72] A. Ishihara, S. Doi, S. Mitsushima, K.-i. Ota, *Electrochim. Acta* **2008**, *53*, 5442 – 5450.
[73] A. Ishihara, K. Lee, S. Doi, S. Mitsushima, N. Kamiya, M. Hara, K. Domen, K. Fukuda, K.-U. Ota, *Electrochem. Solid-State Lett.* **2005**, *8*, A201.
[74] S. Doi, A. Ishihara, S. Mitsushima, N. Kamiya, K.-i. Ota, *J. Electrochem. Soc.* **2007**, *154*, B362.
[75] B. Cao, G. M. Veith, R. E. Diaz, J. Liu, E. A. Stach, R. R. Adzic, P. G. Khalifah, *Angew. Chem. Int. Ed.* **2013**, *52*, 10753 – 10757; *Angew. Chem.* **2013**, *125*, 10953 – 10957.
[76] J. Liu, L. Jiang, B. Zhang, J. Jin, D. S. Su, S. Wang, G. Sun, *ACS Catal.* **2014**, *4*, 2998 – 3001.
[77] J. Xu, P. Gao, T. S. Zhao, *Energy Environ. Sci.* **2012**, *5*, 5333 – 5339.
[78] Y. J. Sa, K. Kwon, J. Y. Cheon, F. Kleitz, S. H. Joo, *J. Mater. Chem. A* **2013**, *1*, 9992 – 10001.
[79] S. Guo, S. Zhang, L. Wu, S. Sun, *Angew. Chem. Int. Ed.* **2012**, *51*, 11770 – 11773; *Angew. Chem.* **2012**, *124*, 11940 – 11943.
[80] W. Xia, R. Zou, L. An, D. Xia, S. Guo, *Energy Environ. Sci.* **2015**, *8*, 568 – 576.
[81] J. Xiao, C. Chen, J. Xi, Y. Xu, F. Xiao, S. Wang, S. Yang, *Nanoscale* **2015**, *7*, 7056 – 7064.
[82] M. Fayette, A. Nelson, R. D. Robinson, *J. Mater. Chem. A* **2015**, *3*, 4274 – 4283.

[83] Y. Wu, Q. Shi, Y. Li, Z. Lai, H. Yu, H. Wang, F. Peng, *J. Mater. Chem. A* **2015**, *3*, 1142 – 1151.
[84] B. Li, X. Ge, F. W. T. Goh, T. S. A. Hor, D. Geng, G. Du, Z. Liu, J. Zhang, X. Liu, Y. Zong, *Nanoscale* **2015**, *7*, 1830 – 1838.
[85] Y. Liang, H. Wang, P. Diao, W. Chang, G. Hong, Y. Li, M. Gong, L. Xie, J. Zhou, J. Wang, T. Z. Regier, F. Wei, H. Dai, *J. Am. Chem. Soc.* **2012**, *134*, 15849 – 15857.
[86] Y. Li, M. Gong, Y. Liang, J. Feng, J. E. Kim, H. Wang, G. Hong, B. Zhang, H. Dai, *Nat. Commun.* **2013**, *4*, 1805.
[87] Y. Liang, Y. Li, H. Wang, J. Zhou, J. Wang, T. Regier, H. Dai, *Nat. Mater.* **2011**, *10*, 780 – 786.
[88] S. Mao, Z. Wen, T. Huang, Y. Hou, J. Chen, *Energy Environ. Sci.* **2014**, *7*, 609 – 616.
[89] C.-H. Kuo, I. M. Mosa, S. Thanneeru, V. Sharma, L. Zhang, S. Biswas, M. Aindow, S. Pamir Alpay, J. F. Rusling, S. L. Suib, J. He, *Chem. Commun.* **2015**, *51*, 5951 – 5954.
[90] Y. Tan, C. Xu, G. Chen, X. Fang, N. Zheng, Q. Xie, *Adv. Funct. Mater.* **2012**, *22*, 4584 – 4591.
[91] Y. Gorlin, T. F. Jaramillo, *J. Am. Chem. Soc.* **2010**, *132*, 13612 – 13614.
[92] K. L. Pickrahn, S. W. Park, Y. Gorlin, H.-B.-R. Lee, T. F. Jaramillo, S. F. Bent, *Adv. Energy Mater.* **2012**, *2*, 1269 – 1277.
[93] J. Duan, S. Chen, S. Dai, S. Z. Qiao, *Adv. Funct. Mater.* **2014**, *24*, 2072 – 2078.
[94] Y.-g. Wang, L. Cheng, F. Li, H.-m. Xiong, Y.-y. Xia, *Chem. Mater.* **2007**, *19*, 2095 – 2101.
[95] F. Cheng, T. Zhang, Y. Zhang, J. Du, X. Han, J. Chen, *Angew. Chem. Int. Ed.* **2013**, *52*, 2474 – 2477; *Angew. Chem.* **2013**, *125*, 2534 – 2537.
[96] T. Zhang, F. Cheng, J. Du, Y. Hu, J. Chen, *Adv. Energy Mater.* **2015**, *5*, 1400654.
[97] L. Mao, *Electrochim. Acta* **2003**, *48*, 1015 – 1021.
[98] W. Sun, A. Hsu, R. Chen, *J. Power Sources* **2011**, *196*, 627 – 635.
[99] F. H. B. Lima, M. L. Calegaro, E. A. Ticianelli, *J. Electroanal. Chem.* **2006**, *590*, 152 – 160.
[100] J. P. Brenet, *J. Power Sources* **1979**, *4*, 183 – 190.
[101] Z. S. Wu, S. Yang, Y. Sun, K. Parvez, X. Feng, K. Müllen, *J. Am. Chem. Soc.* **2012**, *134*, 9082 – 9085.
[102] Y. Su, H. Jiang, Y. Zhu, X. Yang, J. Shen, W. Zou, J. Chen, C. Li, *J. Mater. Chem. A* **2014**, *2*, 7281 – 7287.
[103] X. Y. Yan, X. L. Tong, Y. F. Zhang, X. D. Han, Y. Y. Wang, G. Q. Jin, Y. Qin, X. Y. Guo, *Chem. Commun.* **2012**, *48*, 1892 – 1894.
[104] R. Zhou, Y. Zheng, D. Hulicova-Jurcakova, S. Z. Qiao, *J. Mater. Chem. A* **2013**, *1*, 13179 – 13185.
[105] J.-H. Kim, A. Ishihara, S. Mitsushima, N. Kamiya, K.-I. Ota, *Electrochim. Acta* **2007**, *52*, 2492 – 2497.
[106] Y. Takasu, M. Suzuki, H. Yang, T. Ohashi, W. Sugimoto, *Electrochim. Acta* **2010**, *55*, 8220 – 8229.
[107] Y. Liu, A. Ishihara, S. Mitsushima, N. Kamiya, K.-i. Ota, *Electrochem. Solid-State Lett.* **2005**, *8*, A400.
[108] J. Seo, D. Cha, K. Takanabe, J. Kubota, K. Domen, *Chem. Commun.* **2012**, *48*, 9074 – 9076.
[109] K. Sasaki, L. Zhang, R. R. Adzic, *Phys. Chem. Chem. Phys.* **2008**, *10*, 159 – 167.
[110] Y. Liu, A. Ishihara, S. Mitsushima, N. Kamiya, K.-i. Ota, *J. Electrochem. Soc.* **2007**, *154*, B664.
[111] T. Hyodo, M. Hayashi, N. Miura, N. Yamazoe, *J. Electrochem. Soc.* **1996**, *143*, L266 – L267.
[112] Z. Zhang, J. Liu, J. Gu, L. Su, L. Cheng, *Energy Environ. Sci.* **2014**, *7*, 2535 – 2558.
[113] R. F. Savinell, *Nat. Chem.* **2011**, *3*, 501 – 502.
[114] E. Fabbri, R. Mohamed, P. Levecque, O. Conrad, R. Kötz, T. J. Schmidt, *ChemElectroChem* **2014**, *1*, 338 – 342.
[115] M. Risch, K. A. Stoerzinger, S. Maruyama, W. T. Hong, I. Takeuchi, Y. Shao-Horn, *J. Am. Chem. Soc.* **2014**, *136*, 5229 – 5232.
[116] J. Suntivich, H. A. Gasteiger, N. Yabuuchi, H. Nakanishi, J. B. Goodenough, Y. Shao-Horn, *Nat. Chem.* **2011**, *3*, 546 – 550.
[117] M. Hamdani, R. N. Singh, P. Chartier, *Int. J. Electrochem. Sci.* **2010**, *5*, 556 – 577.
[118] G. Zhang, B. Y. Xia, X. Wang, X. W. David Lou, *Adv. Mater.* **2014**, *26*, 2408 – 2412.
[119] Y. Liang, H. Wang, J. Zhou, Y. Li, J. Wang, T. Regier, H. Dai, *J. Am. Chem. Soc.* **2012**, *134*, 3517 – 3523.
[120] F. Cheng, J. Shen, B. Peng, Y. Pan, Z. Tao, J. Chen, *Nat. Chem.* **2011**, *3*, 79 – 84.
[121] H. Zhu, S. Zhang, Y. X. Huang, L. Wu, S. Sun, *Nano Lett.* **2013**, *13*, 2947 – 2951.
[122] M. S. Faber, S. Jin, *Energy Environ. Sci.* **2014**, *7*, 3519 – 3542.
[123] J. Yang, J. J. Xu, *Electrochem. Commun.* **2003**, *5*, 306 – 311.
[124] J. S. Lee, G. S. Park, H. I. Lee, S. T. Kim, R. Cao, M. Liu, J. Cho, *Nano Lett.* **2011**, *11*, 5362 – 5366.
[125] A. Indra, P. W. Menezes, N. R. Sahraie, A. Bergmann, C. Das, M. Tallarida, D. Schmeißer, P. Strasser, M. Driess, *J. Am. Chem. Soc.* **2014**, *136*, 17530 – 17536.
[126] K. Lee, N. Alonso-Vante, J. Zhang, *Non-Noble Metal Fuel Cell Catalysts*, Wiley-VCH, Weinheim, **2014**, pp. 157 – 182.
[127] D. Baresel, W. Sarholz, P. Scharner, J. Schmitz, *Ber. Bunsen-Ges.* **1974**, *78*, 608 – 611.
[128] H. Behret, H. Binder, G. Sandstede, *Electrochim. Acta* **1975**, *20*, 111 – 117.
[129] Y. X. Zhou, H. B. Yao, Y. Wang, H. L. Liu, M. R. Gao, P. K. Shen, S. H. Yu, *Chem. Eur. J.* **2010**, *16*, 12000 – 12007.
[130] H. Wang, Y. Liang, Y. Li, H. Dai, *Angew. Chem. Int. Ed.* **2011**, *50*, 10969 – 10972; *Angew. Chem.* **2011**, *123*, 11161 – 11164.
[131] Z. Zhang, X. Wang, G. Cui, A. Zhang, X. Zhou, H. Xu, L. Gu, *Nanoscale* **2014**, *6*, 3540 – 3544.
[132] M. Shen, C. Ruan, Y. Chen, C. Jiang, K. Ai, L. Lu, *ACS Appl. Mater. Interfaces* **2015**, *7*, 1207 – 1218.
[133] R. Jasinski, *Nature* **1964**, *201*, 1212 – 1213.
[134] A. A. Tanaka, C. Fierro, D. Scherson, E. B. Yaeger, *J. Phys. Chem.* **1987**, *91*, 3799 – 3807.
[135] V. S. Bagotzky, M. R. Tarasevich, K. A. Radyushkina, O. A. Levina, S. I. Andrusyova, *J. Power Sources* **1978**, *2*, 233 – 240.
[136] C. W. B. Bezerra, L. Zhang, H. Liu, K. Lee, A. L. B. Marques, E. P. Marques, H. Wang, J. Zhang, *J. Power Sources* **2007**, *173*, 891 – 908.
[137] S. Gupta, D. Tryk, I. Bae, W. Aldred, E. Yeager, *J. Appl. Electrochem.* **1989**, *19*, 19 – 27.
[138] C. W. B. Bezerra, L. Zhang, K. Lee, H. Liu, A. L. B. Marques, E. P. Marques, H. Wang, J. Zhang, *Electrochim. Acta* **2008**, *53*, 4937 – 4951.
[139] M. Lefèvre, E. Proietti, F. Jaouen, J.-P. Dodelet, *Science* **2009**, *324*, 71 – 74.
[140] G. Wu, K. L. More, C. M. Johnston, P. Zelenay, *Science* **2011**, *332*, 443 – 447.
[141] F. Jaouen, S. Marcotte, J.-P. Dodelet, G. Lindbergh, *J. Phys. Chem. B* **2003**, *107*, 1376 – 1386.
[142] Y. Zhu, B. Zhang, X. Liu, D. W. Wang, D. S. Su, *Angew. Chem. Int. Ed.* **2014**, *53*, 10673 – 10677; *Angew. Chem.* **2014**, *126*, 10849 – 10853.
[143] V. Nallathambi, J.-W. Lee, S. P. Kumaraguru, G. Wu, B. N. Popov, *J. Power Sources* **2008**, *183*, 34 – 42.
[144] G. Wu, N. H. Mack, W. Gao, S. Ma, R. Zhong, J. Han, J. K. Baldwin, P. Zelenay, *ACS Nano* **2012**, *6*, 9764 – 9776.
[145] J. Masa, W. Xia, I. Sinev, A. Zhao, Z. Sun, S. Grutzke, P. Weide, M. Muhler, W. Schuhmann, *Angew. Chem. Int. Ed.* **2014**, *53*, 8508 – 8512; *Angew. Chem.* **2014**, *126*, 8648 – 8652.
[146] G. Wu, P. Zelenay, *Acc. Chem. Res.* **2013**, *46*, 1878 – 1889.
[147] Z. S. Wu, L. Chen, J. Liu, K. Parvez, H. Liang, J. Shu, H. Sachdev, R. Graf, X. Feng, K. Müllen, *Adv. Mater.* **2014**, *26*, 1450 – 1455.

[148] H. W. Liang, W. Wei, Z. S. Wu, X. Feng, K. Müllen, *J. Am. Chem. Soc.* **2013**, *135*, 16002 – 16005.
[149] W. Yang, X. Liu, X. Yue, J. Jia, S. Guo, *J. Am. Chem. Soc.* **2015**, *137*, 1436 – 1439.
[150] Z. Xiang, Y. Xue, D. Cao, L. Huang, J. F. Chen, L. Dai, *Angew. Chem. Int. Ed.* **2014**, *53*, 2433 – 2437; *Angew. Chem.* **2014**, *126*, 2465 – 2469.
[151] S. Yuan, J.-L. Shui, L. Grabstanowicz, C. Chen, S. Commet, B. Reprogle, T. Xu, L. Yu, D.-J. Liu, *Angew. Chem. Int. Ed.* **2013**, *52*, 8349 – 8353; *Angew. Chem.* **2013**, *125*, 8507 – 8511.
[152] S. L. James, *Chem. Soc. Rev.* **2003**, *32*, 276 – 288.
[153] J. L. C. Rowsell, O. M. Yaghi, *Microporous Mesoporous Mater.* **2004**, *73*, 3 – 14.
[154] H. Furukawa, K. E. Cordova, M. O'Keeffe, O. M. Yaghi, *Science* **2013**, *341*, 1230444.
[155] > W. Xia, A. Mahmood, R. Zou, Q. Xu, *Energy Environ. Sci.* **2015**, 1837 – 1866.
[156] W. Xia, J. Zhu, W. Guo, L. An, D. Xia, R. Zou, *J. Mater. Chem. A* **2014**, *2*, 11606 – 11613.
[157] L. Zhang, Z. Su, F. Jiang, L. Yang, J. Qian, Y. Zhou, W. Li, M. Hong, *Nanoscale* **2014**, *6*, 6590 – 6602.
[158] Y. Zhao, J. Zhang, B. Han, J. Song, J. Li, Q. Wang, *Angew. Chem. Int. Ed.* **2011**, *50*, 636 – 639; *Angew. Chem.* **2011**, *123*, 662 – 665.
[159] D. Zhao, J.-L. Shui, C. Chen, X. Chen, B. M. Reprogle, D. Wang, D.-J. Liu, *Chem. Sci.* **2012**, *3*, 3200 – 3205.
[160] S. Ma, G. A. Goenaga, A. V. Call, D. J. Liu, *Chem. Eur. J.* **2011**, *17*, 2063 – 2067.
[161] M. Seredych, E. Rodriguez-Castellon, T. J. Bandosz, *J. Mater. Chem. A* **2014**, *2*, 20164 – 20176.
[162] Y. Hou, T. Huang, Z. Wen, S. Mao, S. Cui, J. Chen, *Adv. Energy Mater.* **2014**, *4*, 1400337.
[163] A. Kong, Q. Lin, C. Mao, X. P. Feng, *Chem. Commun.* **2014**, *50*, 15619 – 15622.
[164] A. Aijaz, N. Fujiwara, Q. Xu, *J. Am. Chem. Soc.* **2014**, *136*, 6790 – 6793.
[165] B. Liu, H. Shioyama, T. Akita, Q. Xu, *J. Am. Chem. Soc.* **2008**, *130*, 5390 – 5391.
[166] X. Zhao, H. Zhao, T. Zhang, X. Yan, Y. Yuan, H. Zhang, H. Zhao, D. Zhang, G. Zhu, X. Yao, *J. Mater. Chem. A* **2014**, *2*, 11666 – 11671.
[167] J. Li, Y. Chen, Y. Tang, S. Li, H. Dong, K. Li, M. Han, Y.-Q. Lan, J. Bao, Z. Dai, *J. Mater. Chem. A* **2014**, *2*, 6316 – 6319.
[168] J. S. Li, S. L. Li, Y. J. Tang, K. Li, L. Zhou, N. Kong, Y. Q. Lan, J. C. Bao, Z. H. Dai, *Sci. Rep.* **2014**, *4*, 5130.
[169] Q. Li, P. Xu, W. Gao, S. Ma, G. Zhang, R. Cao, J. Cho, H. L. Wang, G. Wu, *Adv. Mater.* **2014**, *26*, 1378 – 1386.
[170] W. Zhang, Z. Y. Wu, H. L. Jiang, S. H. Yu, *J. Am. Chem. Soc.* **2014**, *136*, 14385 – 14388.
[171] T. Y. Ma, S. Dai, M. Jaroniec, S. Z. Qiao, *J. Am. Chem. Soc.* **2014**, *136*, 13925 – 13931.
[172] H. Shi, Y. Shen, F. He, Y. Li, A. Liu, S. Liu, Y. Zhang, *J. Mater. Chem. A* **2014**, *2*, 15704 – 15716.
[173] J. Tang, J. Liu, N. L. Torad, T. Kimura, Y. Yamauchi, *Nano Today* **2014**, *9*, 305 – 323.
[174] S. Chen, J. Bi, Y. Zhao, L. Yang, C. Zhang, Y. Ma, Q. Wu, X. Wang, Z. Hu, *Adv. Mater.* **2012**, *24*, 5593 – 5597.
[175] W. He, C. Jiang, J. Wang, L. Lu, *Angew. Chem. Int. Ed.* **2014**, *53*, 9503 – 9507; *Angew. Chem.* **2014**, *126*, 9657 – 9661.
[176] H. Li, W. Kang, L. Wang, Q. Yue, S. Xu, H. Wang, J. Liu, *Carbon* **2013**, *54*, 249 – 257.
[177] Z. Zhang, G. M. Veith, G. M. Brown, P. F. Fulvio, P. C. Hillesheim, S. Dai, S. H. Overbury, *Chem. Commun.* **2014**, *50*, 1469 – 1471.
[178] H. Jin, H. Zhang, H. Zhong, J. Zhang, *Energy Environ. Sci.* **2011**, *4*, 3389 – 3394.
[179] Y. Zhang, J. Ge, L. Wang, D. Wang, F. Ding, X. Tao, W. Chen, *Sci. Rep.* **2013**, *3*, 2771.
[180] H. Nie, Y. Zhang, W. Zhou, J. Li, B. Wu, T. Liu, H. Zhang, *Electrochim. Acta* **2014**, *150*, 205 – 210.
[181] C. Zhang, R. Hao, H. Liao, Y. Hou, *Nano Energy* **2013**, *2*, 88 – 97.
[182] E. J. Biddinger, U. S. Ozkan, *J. Phys. Chem. C* **2010**, *114*, 15306 – 15314.
[183] X. Sun, Y. Zhang, P. Song, J. Pan, L. Zhuang, W. Xu, W. Xing, *ACS Catal.* **2013**, *3*, 1726 – 1729.
[184] S. Inamdar, H.-S. Choi, P. Wang, M. Y. Song, J.-S. Yu, *Electrochem. Commun.* **2013**, *30*, 9 – 12.
[185] D. S. Yang, D. Bhattacharjya, S. Inamdar, J. Park, J. S. Yu, *J. Am. Chem. Soc.* **2012**, *134*, 16127 – 16130.
[186] C. H. Choi, S. H. Park, S. I. Woo, *ACS Nano* **2012**, *6*, 7084 – 7091.
[187] H. Wang, X. Bo, Y. Zhang, L. Guo, *Electrochim. Acta* **2013**, *108*, 404 – 411.
[188] J. Wang, Z. Xu, Y. Gong, C. Han, H. Li, Y. Wang, *ChemCatChem* **2014**, *6*, 1204 – 1209.
[189] Y. Meng, D. Voiry, A. Goswami, X. Zou, X. Huang, M. Chhowalla, Z. Liu, T. Asefa, *J. Am. Chem. Soc.* **2014**, *136*, 13554 – 13557.
[190] R. Silva, D. Voiry, M. Chhowalla, T. Asefa, *J. Am. Chem. Soc.* **2013**, *135*, 7823 – 7826.
[191] J. Tang, J. Liu, C. Li, Y. Li, M. O. Tade, S. Dai, Y. Yamauchi, *Angew. Chem. Int. Ed.* **2015**, *54*, 588 – 593; *Angew. Chem.* **2015**, *127*, 598 – 603.
[192] H.-W. Liang, X. Zhuang, S. Brüller, X. Feng, K. Müllen, *Nat. Commun.* **2014**, *5*, 4973.
[193] S. Iijima, *Nature* **1991**, *354*, 56 – 58.
[194] Y. Yan, J. Miao, Z. Yang, F.-X. Xiao, H. B. Yang, B. Liu, Y. Yang, *Chem. Soc. Rev.* **2015**, *44*, 3295 – 3346.
[195] M. D. Esrafili, *Comput. Theor. Chem.* **2013**, *1015*, 1 – 7.
[196] K. Waki, R. A. Wong, H. S. Oktaviano, T. Fujio, T. Nagai, K. Kimoto, K. Yamada, *Energy Environ. Sci.* **2014**, *7*, 1950 – 1958.
[197] Z. Shi, J. Zhang, Z.-S. Liu, H. Wang, D. P. Wilkinson, *Electrochim. Acta* **2006**, *51*, 1905 – 1916.
[198] Q. Li, R. Cao, J. Cho, G. Wu, *Adv. Energy Mater.* **2014**, *4*, 1301415.
[199] K. Gong, F. Du, Z. Xia, M. Durstock, L. Dai, *Science* **2009**, *323*, 760 – 764.
[200] Y. Li, W. Zhou, H. Wang, L. Xie, Y. Liang, F. Wei, J.-C. Idrobo, S. J. Pennycook, H. Dai, *Nat. Nanotechnol.* **2012**, *7*, 394 – 400.
[201] L. Yang, S. Jiang, Y. Zhao, L. Zhu, S. Chen, X. Wang, Q. Wu, J. Ma, Y. Ma, Z. Hu, *Angew. Chem. Int. Ed.* **2011**, *50*, 7132 – 7135; *Angew. Chem.* **2011**, *123*, 7270 – 7273.
[202] Z. Liu, F. Peng, H. Wang, H. Yu, J. Tan, L. Zhu, *Catal. Commun.* **2011**, *16*, 35 – 38.
[203] W. Li, D. Yang, H. Chen, Y. Gao, H. Li, *Electrochim. Acta* **2015**, *165*, 191 – 197.
[204] Y. Zhao, L. Yang, S. Chen, X. Wang, Y. Ma, Q. Wu, Y. Jiang, W. Qian, Z. Hu, *J. Am. Chem. Soc.* **2013**, *135*, 1201 – 1204.
[205] G.-L. Tian, Q. Zhang, B. Zhang, Y.-G. Jin, J.-Q. Huang, D. S. Su, F. Wei, *Adv. Funct. Mater.* **2014**, *24*, 5956 – 5961.
[206] Q. Li, N. Mahmood, J. Zhu, Y. Hou, S. Sun, *Nano Today* **2014**, *9*, 668 – 683.
[207] J. Jin, F. Pan, L. Jiang, X. Fu, A. Liang, Z. Wei, J. Zhang, G. Sun, *ACS Nano* **2014**, *8*, 3313 – 3321.
[208] C. Zhang, N. Mahmood, H. Yin, F. Liu, Y. Hou, *Adv. Mater.* **2013**, *25*, 4932 – 4937.
[209] S. Yang, L. Zhi, K. Tang, X. Feng, J. Maier, K. Müllen, *Adv. Funct. Mater.* **2012**, *22*, 3634 – 3640.
[210] J. Liang, Y. Jiao, M. Jaroniec, S. Z. Qiao, *Angew. Chem. Int. Ed.* **2012**, *51*, 11496 – 11500; *Angew. Chem.* **2012**, *124*, 11664 – 11668.
[211] X. Wang, G. Sun, P. Routh, D.-H. Kim, W. Huang, P. Chen, *Chem. Soc. Rev.* **2014**, *43*, 7067 – 7098.

[212] I.-Y. Jeon, D. Yu, S.-Y. Bae, H.-J. Choi, D. W. Chang, L. Dai, J.-B. Baek, *Chem. Mater.* **2011**, *23*, 3987 – 3992.
[213] I. Y. Jeon, H. J. Choi, S. M. Jung, J. M. Seo, M. J. Kim, L. Dai, J. B. Baek, *J. Am. Chem. Soc.* **2013**, *135*, 1386 – 1393.
[214] I. Y. Jeon, S. Zhang, L. Zhang, H. J. Choi, J. M. Seo, Z. Xia, L. Dai, J. B. Baek, *Adv. Mater.* **2013**, *25*, 6138 – 6145.
[215] Z. Ma, S. Dou, A. Shen, L. Tao, L. Dai, S. Wang, *Angew. Chem. Int. Ed.* **2015**, *54*, 1888 – 1892; *Angew. Chem.* **2015**, *127*, 1908 – 1912.
[216] L. Wang, Z. Sofer, A. Ambrosi, P. Šimek, M. Pumera, *Electrochem. Commun.* **2014**, *46*, 148 – 151.
[217] Y. Zhao, C. Hu, L. Song, L. Wang, G. Shi, L. Dai, L. Qu, *Energy Environ. Sci.* **2014**, *7*, 1913 – 1918.
[218] C. J. Shearer, A. Cherevan, D. Eder, *Adv. Mater.* **2014**, *26*, 2295 – 2318.
[219] D. Deng, L. Yu, X. Chen, G. Wang, L. Jin, X. Pan, J. Deng, G. Sun, X. Bao, *Angew. Chem. Int. Ed.* **2013**, *52*, 371 – 375; *Angew. Chem.* **2013**, *125*, 389 – 393.
[220] A. Zhao, J. Masa, W. Xia, A. Maljusch, M. G. Willinger, G. Clavel, K. Xie, R. Schlogl, W. Schuhmann, M. Muhler, *J. Am. Chem. Soc.* **2014**, *136*, 7551 – 7554.
[221] X. Zhou, Z. Tian, J. Li, H. Ruan, Y. Ma, Z. Yang, Y. Qu, *Nanoscale* **2014**, *6*, 2603 – 2607.
[222] H. Fei, R. Ye, G. Ye, Y. Gong, Z. Peng, X. Fan, E. L. G. Samuel, P. M. Ajayan, J. M. Tour, *ACS Nano* **2014**, *8*, 10837 – 10843.
[223] Y. J. Sa, C. Park, H. Y. Jeong, S. H. Park, Z. Lee, K. T. Kim, G. G. Park, S. H. Joo, *Angew. Chem. Int. Ed.* **2014**, *53*, 4102 – 4106; *Angew. Chem.* **2014**, *126*, 4186 – 4190.
[224] T. Y. Ma, J. Ran, S. Dai, M. Jaroniec, S. Z. Qiao, *Angew. Chem. Int. Ed.* **2015**, *54*, 4646 – 4650; *Angew. Chem.* **2015**, *127*, 4729 – 4733.
[225] Y. Zheng, Y. Jiao, J. Chen, J. Liu, J. Liang, A. Du, W. Zhang, Z. Zhu, S. C. Smith, M. Jaroniec, G. Q. Lu, S. Z. Qiao, *J. Am. Chem. Soc.* **2011**, *133*, 20116 – 20119.
[226] Q. Guo, D. Zhao, S. Liu, S. Chen, M. Hanif, H. Hou, *Electrochim. Acta* **2014**, *138*, 318 – 324.
[227] S. Yang, X. Feng, X. Wang, K. Müllen, *Angew. Chem. Int. Ed.* **2011**, *50*, 5339 – 5343; *Angew. Chem.* **2011**, *123*, 5451 – 5455.
[228] Z. Wen, S. Ci, Y. Hou, J. Chen, *Angew. Chem. Int. Ed.* **2014**, *53*, 6496 – 6500; *Angew. Chem.* **2014**, *126*, 6614 – 6618.
[229] G. L. Tian, M. Q. Zhao, D. Yu, X. Y. Kong, J. Q. Huang, Q. Zhang, F. Wei, *Small* **2014**, *10*, 2251 – 2259.
[230] T. N. Ye, L. B. Lv, X. H. Li, M. Xu, J. S. Chen, *Angew. Chem. Int. Ed.* **2014**, *53*, 6905 – 6909; *Angew. Chem.* **2014**, *126*, 7025 – 7029.
[231] S. E. F. Kleijn, S. C. S. Lai, M. T. M. Koper, P. R. Unwin, *Angew. Chem. Int. Ed.* **2014**, *53*, 3558 – 3586; *Angew. Chem.* **2014**, *126*, 3630 – 3660.
[232] W. Wang, N. Tao, *Anal. Chem.* **2014**, *86*, 2 – 14.
[233] X. Xiao, A. J. Bard, *J. Am. Chem. Soc.* **2007**, *129*, 9610 – 9612.
[234] R. Dasari, D. A. Robinson, K. J. Stevenson, *J. Am. Chem. Soc.* **2013**, *135*, 570 – 573.
[235] Z. Guo, S. J. Percival, B. Zhang, *J. Am. Chem. Soc.* **2014**, *136*, 8879 – 8882.
[236] C. M. Sánchez-Sánchez, J. Solla-Gullón, F. J. Vidal-Iglesias, A. Aldaz, V. Montiel, E. Herrero, *J. Am. Chem. Soc.* **2010**, *132*, 5622 – 5624.
[237] T. Sun, Y. Yu, B. J. Zacher, M. V. Mirkin, *Angew. Chem. Int. Ed.* **2014**, *53*, 14120 – 14123; *Angew. Chem.* **2014**, *126*, 14344 – 14347.
[238] Y. Li, D. Bergman, B. Zhang, *Anal. Chem.* **2009**, *81*, 5496 – 5502.
[239] X. Shan, U. Patel, S. Wang, R. Iglesias, N. Tao, *Science* **2010**, *327*, 1363 – 1366.
[240] X. Shan, I. Diez-Perez, L. Wang, P. Wiktor, Y. Gu, L. Zhang, W. Wang, J. Lu, S. Wang, Q. Gong, J. Li, N. Tao, *Nat. Nanotechnol.* **2012**, *7*, 668 – 672.
[241] X. Zhou, N. M. Andoy, G. Liu, E. Choudhary, K.-S. Han, H. Shen, P. Chen, *Nat. Nanotechnol.* **2012**, *7*, 237 – 241.
[242] P. Chen, X. Zhou, N. M. Andoy, K. S. Han, E. Choudhary, N. Zou, G. Chen, H. Shen, *Chem. Soc. Rev.* **2014**, *43*, 1107 – 1117.
[243] A. J. Wain, *Electrochim. Acta* **2013**, *92*, 383 – 391.
[244] J. L. Fernández, M. Wijesinghe, C. G. Zoski, *Anal. Chem.* **2015**, *87*, 1066 – 1074.
[245] J. L. Fernández, D. A. Walsh, A. J. Bard, *J. Am. Chem. Soc.* **2005**, *127*, 357 – 365.
[246] J. C. Byers, A. G. Guell, P. R. Unwin, *J. Am. Chem. Soc.* **2014**, *136*, 11252 – 11255.
[247] N. Ebejer, M. Schnippering, A. W. Colburn, M. A. Edwards, P. R. Unwin, *Anal. Chem.* **2010**, *82*, 9141 – 9145.
[248] A. Shen, Y. Zou, Q. Wang, R. A. Dryfe, X. Huang, S. Dou, L. Dai, S. Wang, *Angew. Chem. Int. Ed.* **2014**, *53*, 10804 – 10808; *Angew. Chem.* **2014**, *126*, 10980 – 10984.
[249] T. Palaniselvam, M. O. Valappil, R. Illathvalappil, S. Kurungot, *Energy Environ. Sci.* **2014**, *7*, 1059 – 1067.
[250] G. L. Chai, Z. Hou, D. J. Shu, T. Ikeda, K. Terakura, *J. Am. Chem. Soc.* **2014**, *136*, 13629 – 13640.
[251] H. Kim, K. Lee, S. I. Woo, Y. Jung, *Phys. Chem. Chem. Phys.* **2011**, *13*, 17505 – 17510.
[252] C. E. Banks, T. J. Davies, G. G. Wildgoose, R. G. Compton, *Chem. Commun.* **2005**, 829 – 841.
[253] P. S. Toth, A. T. Valota, M. Velický, I. A. Kinloch, K. S. Novoselov, E. W. Hill, R. A. W. Dryfe, *Chem. Sci.* **2014**, *5*, 582 – 589.

Received: May 28, 2015
Published online: December 14, 2015

